Kepler 's First Rocky Planet: Kepler-10b

The Astrophysical Journal, 729:27 (21pp), 2011 March 1 doi:10.1088/0004-637X/729/1/27

KEPLER'S FIRST ROCKY PLANET: KEPLER-10b*

Natalie M. Batalha[1], William J. Borucki[2], Stephen T. Bryson[2], Lars A. Buchhave[3], Douglas A. Caldwell[4], Jørgen Christensen-Dalsgaard[5,6], David Ciardi[7], Edward W. Dunham[8], Francois Fressin[3], Thomas N. Gautier III[9], Ronald L. Gilliland[10], Michael R. Haas[2], Steve B. Howell[11], Jon M. Jenkins[4], Hans Kjeldsen[5], David G. Koch[2], David W. Latham[3], Jack J. Lissauer[2], Geoffrey W. Marcy[12], Jason F. Rowe[2], Dimitar D. Sasselov[3], Sara Seager[13], Jason H. Steffen[14], Guillermo Torres[3], Gibor S. Basri[12], Timothy M. Brown[15], David Charbonneau[3], Jessie Christiansen[2], Bruce Clarke[4], William D. Cochran[16], Andrea Dupree[3], Daniel C. Fabrycky[3], Debra Fischer[17], Eric B. Ford[18], Jonathan Fortney[19], Forrest R. Girouard[20], Matthew J. Holman[3], John Johnson[21], Howard Isaacson[12], Todd C. Klaus[20], Pavel Machalek[4], Althea V. Moorehead[18], Robert C. Morehead[18], Darin Ragozzine[3], Peter Tenenbaum[4], Joseph Twicken[4], Samuel Quinn[3], Jeffrey VanCleve[4], Lucianne M. Walkowicz[12], William F. Welsh[22], Edna Devore[4], and Alan Gould[23]

[1] Department of Physics and Astronomy, San Jose State University, San Jose, CA 95192, USA; Natalie.Batalha@sjsu.edu
[2] NASA Ames Research Center, Moffett Field, CA 94035, USA
[3] Harvard-Smithsonian Center for Astrophysics, 60 Garden Street, Cambridge, MA 02138, USA
[4] SETI Institute/NASA Ames Research Center, Moffett Field, CA 94035, USA
[5] Department of Physics and Astronomy, Aarhus University, DK-8000 Aarhus C, Denmark
[6] High Altitude Observatory, National Center for Atmospheric Research, Boulder, CO 80307, USA
[7] NASA Exoplanet Science Institute/Caltech, Pasadena, CA 91125, USA
[8] Lowell Observatory, Flagstaff, AZ 86001, USA
[9] Jet Propulsion Laboratory/California Institute of Technology, Pasadena, CA 91109, USA
[10] Space Telescope Science Institute, Baltimore, MD 21218, USA
[11] National Optical Astronomy Observatory, Tucson, AZ 85719, USA
[12] Department of Astronomy, University of California, Berkeley, Berkeley, CA 94720, USA
[13] Massachusetts Institute of Technology, Cambridge, MA 02139, USA
[14] Fermilab Center for Particle Astrophysics, Batavia, IL 60510, USA
[15] Las Cumbres Observatory Global Telescope, Goleta, CA 93117, USA
[16] Department of Astronomy, University of Texas, Austin, TX 78712, USA
[17] Department of Astronomy, Yale University, New Haven, CT 06510, USA
[18] Department of Astronomy, University of Florida, Gainesville, FL 32611, USA
[19] Department of Astronomy and Astrophysics, University of California, Santa Cruz, Santa Cruz, CA 95064, USA
[20] Orbital Sciences Corp., NASA Ames Research Center, Moffett Field, CA 94035, USA
[21] California Institute of Technology, Pasadena, CA 91109, USA
[22] Department of Astronomy, San Diego State University, San Diego, CA 92182, USA
[23] Lawrence Hall of Science, Berkeley, CA 94720, USA
Received 2010 November 10; accepted 2010 November 25; published 2011 February 7

ABSTRACT

NASA's *Kepler* Mission uses transit photometry to determine the frequency of Earth-size planets in or near the habitable zone of Sun-like stars. The mission reached a milestone toward meeting that goal: the discovery of its first rocky planet, Kepler-10b. Two distinct sets of transit events were detected: (1) a 152 ± 4 ppm dimming lasting 1.811 ± 0.024 hr with ephemeris $T\,[\mathrm{BJD}] = 2454964.57375^{+0.00060}_{-0.00082} + N * 0.837495^{+0.000004}_{-0.000005}$ days and (2) a 376 ± 9 ppm dimming lasting 6.86 ± 0.07 hr with ephemeris $T\,[\mathrm{BJD}] = 2454971.6761^{+0.0020}_{-0.0023} + N * 45.29485^{+0.00065}_{-0.00076}$ days. Statistical tests on the photometric and pixel flux time series established the viability of the planet candidates triggering ground-based follow-up observations. Forty precision Doppler measurements were used to confirm that the short-period transit event is due to a planetary companion. The parent star is bright enough for asteroseismic analysis. Photometry was collected at 1 minute cadence for >4 months from which we detected 19 distinct pulsation frequencies. Modeling the frequencies resulted in precise knowledge of the fundamental stellar properties. Kepler-10 is a relatively old (11.9 ± 4.5 Gyr) but otherwise Sun-like main-sequence star with $T_{\mathrm{eff}} = 5627 \pm 44$ K, $M_\star = 0.895 \pm 0.060\,M_\odot$, and $R_\star = 1.056 \pm 0.021\,R_\odot$. Physical models simultaneously fit to the transit light curves and the precision Doppler measurements yielded tight constraints on the properties of Kepler-10b that speak to its rocky composition: $M_{\mathrm{P}} = 4.56^{+1.17}_{-1.29}\,M_\oplus$, $R_{\mathrm{P}} = 1.416^{+0.033}_{-0.036}\,R_\oplus$, and $\rho_{\mathrm{P}} = 8.8^{+2.1}_{-2.9}$ g cm^{-3}. Kepler-10b is the smallest transiting exoplanet discovered to date.

Key words: planetary systems – stars: individual (Kepler-10, KIC 11904151, 2MASS 19024305+5014286) – techniques: photometric – techniques: spectroscopic

Online-only material: color figures

1. INTRODUCTION

NASA's *Kepler* Mission, launched in 2009 March, uses transit photometry to detect and characterize exoplanets with the objective of determining the frequency of Earth-size planets

* Based in part on observations obtained at the W. M. Keck Observatory, which is operated by the University of California and the California Institute of Technology.

in the habitable zone. The instrument is a wide field-of-view (115 deg^2) photometer comprised of a 0.95 m effective aperture Schmidt telescope feeding an array of 42 CCDs that continuously and simultaneously monitors the brightness of up to 170,000 stars. A comprehensive discussion of the characteristics and on-orbit performance of the instrument and spacecraft is presented in Koch et al. (2010a). The statistical properties of the stars targeted by *Kepler* are described by Batalha et al. (2010a).

In 2010 January, the team announced its first five planet discoveries (Borucki et al. 2010a; Koch et al. 2010b; Dunham et al. 2010; Latham et al. 2010; Jenkins et al. 2010c) identified in the first 43 days of data and confirmed by radial velocity (RV) follow-up. One of these—Kepler-8b—shows a clear Rossiter–McLaughlin velocity variation which allowed for the measurement of the spin–orbit alignment of the system (Jenkins et al. 2010c). The "first five" are all short-period giant planets, the smallest being comparable in size to Neptune. Collectively, they are similar to the sample of transiting exoplanets that have been identified to date,[24] the ranks of which currently hover around 100. The median mass of the sample is 0.99 M_J with a 10th and a 90th percentile of 0.24 M_J and 4.1 M_J. The median radius is 1.18 R_J with a 10th and a 90th percentile of 0.81 R_J and 1.5 R_J. The known transiting planets are, statistically speaking, Jovian-like in both mass and size and have short orbital periods with a median value of 3.5 days and a 10th and a 90th percentile of 1.5 days and 8.0 days, respectively.

In 2010 June, *Kepler* released a catalog of 306 stars with planet-like transit signatures (Borucki et al. 2010b). Even if the majority turn out to be false positives, the number of transiting planets could plausibly more than double from this pool of candidates. Soon, we will leave the realm of small-sample statistics and be able to say something meaningful about not only the mass and size distribution but also the dynamical and compositional nature of exoplanets. Information about composition will fall from those systems for which we can derive not only a radius, but also a mass. Dynamical information will fall from multiple-transiting planet systems. Five such candidate systems were included in the catalog of Borucki et al. (2010b) and described in more detail by Steffen et al. (2010). The discovery of the planets orbiting Kepler-9 (Holman et al. 2010) marked the first confirmation of a multiple-transiting planet system. Kepler-9 is a G-type star with two Saturn-mass transiting planets in a near 2:1 orbital resonance. The system is also the first to show transit timing variations (TTVs). Dynamical models of these variations afford us the means of determining planetary mass without the need for RV follow-up.

After removing the transit signals of Kepler-9b and Kepler-9c, a third transit signature was identified in the light curve revealing an additional candidate with a 1.6 day period. The planetary interpretation of Kepler-9d was validated (Torres et al. 2010) without detection of a Doppler signal. Rather, given the star and transit properties, a matrix of possible false-positive scenarios was constructed. After eliminating all scenarios which are not consistent with the observables, a false-alarm probability was computed that speaks to the likelihood that Kepler-9d is consistent with the planet interpretation. In this manner, Kepler-9d was validated with high confidence as a super-Earth-size planet with radius $1.64^{+0.19}_{-0.14}$ $R_\oplus$.

[24] http://exoplanet.eu/

Here, we attempt to define "super-Earth" from a radius perspective by noting that the 10 $M_\oplus$ upper limit proposed by Valencia et al. (2006) corresponds roughly to 2 $R_\oplus$ for a planet with no water and low Fe/Si ratio (Zeng & Sasselov 2011). Practically speaking, the term super-Earth has been loosely used to refer to all planets larger than Earth and smaller than Neptune. However, this is a broad domain that captures not only rocky, dry planets that happen to be larger than Earth, but also ocean planets and mini-Neptunes. These finer distinctions will only be possible with measurements of planetary properties better than 5% in radius and 10% in mass (Valencia et al. 2006, 2007; Fortney et al. 2007; Seager et al. 2007; Grasset et al. 2009). Pending a mass determination, there is no information as of yet with regards to the composition of Kepler-9d.

The discovery of a short-period, super-Earth-size planet is not surprising. Indeed, one of the most interesting aspects of the *Kepler* candidate sample reported by Borucki et al. (2010b) is the fact that the median of the radius distribution is strikingly different than that of the known transiting exoplanets. The *Kepler* candidates have a median radius of 0.30 R_J—smaller than that of Neptune (0.34 R_J)—and candidates as small as 1.5 $R_\oplus$. Should this distribution survive the process of false positive elimination, we will see substantial numbers of short-period super-Earths. There is precedence already for transiting exoplanet discoveries in the super-Earth domain. CoRoT-7b (Leger et al. 2009; Queloz et al. 2009; Bruntt et al. 2010; Pont et al. 2010) is an example: a 1.58 ± 0.10 $R_\oplus$, 4.8 ± 0.8 $M_\oplus$ planet orbiting a K-type star. The case for CoRoT-7b is complicated by activity-induced RV jitter. Independent analysis of the Doppler measurements by Pont et al. (2010) reduces the significance of the detection somewhat (yielding 2.3 ± 1.8 $M_\oplus$) and puts the 95% confidence interval between 0 and 5 $M_\oplus$—still, however, within the super-Earth domain. And while the Queloz et al. (2009) mass and radius point to a rocky composition, the lower mass of Pont et al. (2010) marginally favors a water/ice composition.

GJ 1214b (Charbonneau et al. 2009) is another example of a transiting super-Earth (as defined from a mass perspective) at 6.55 $M_\oplus$. Orbiting an M-type star with a period of 1.58 days, GJ1214b has a radius of 2.68 $R_\oplus$. Its density (1.87 g cm^{-3}), consequently, is closer to that of water than that of the Earth. The interior structure of GJ 1214b has been modeled as an $H/He/H_2O$ planet with a rocky core (Nettelmann et al. 2010).

Here, we report on the discovery of a super-Earth-size exoplanet orbiting the G-type main-sequence star, Kepler-10 (KIC 11904151). At $Kp = 10.96$, the star is bright enough for asteroseismic analysis of its fundamental stellar properties using the high-precision *Kepler* photometry. The stellar properties are known to an accuracy that allows us to put Kepler-10b sitting squarely in the rocky domain of the mass–radius diagram. The light curve shows two distinct sets of transit events: one at $0.837495^{+0.000004}_{-0.000005}$ days, referred to as KOI-72.01 and the other at $45.29485^{+0.00065}_{-0.00076}$ days, referred to as KOI-72.02 where "KOI" denotes a *Kepler* object of interest.

The Kepler-10 data acquisition, photometry, and transit detection are described in Section 2. The statistical tests performed on the *Kepler* photometry to rule out false positives are described in Section 3, and the subsequent ground-based observations, including precision Doppler measurements, leading to the confirmation of KOI-72.01 are described in Section 4. Throughout the first half of this paper, we refer to each event as KOI-72.01 and KOI-72.02. However, in the latter half, we begin to discuss KOI-72.01 in the context of a confirmed planet and call it out

accordingly as Kepler-10b. The KOI-72.02 signal, at this time, has not been confirmed by RV. Many of the false-positive scenarios have been investigated via BLENDER analysis (Torres et al. 2010) as described in Section 5. KOI-72.02 will require analysis beyond the scope of this paper for validation at an acceptable confidence level, since eliminating possible astrophysical false positives is more difficult given the possibility of an eccentric orbit. The larger orbital separation of KOI-72.02 precludes us from assuming that tidal effects will have circularized the orbit. While both the transit duration and RV observations are consistent with a circular orbit, the uncertainties are large enough that a much more comprehensive BLENDER analysis will be required to validate the outer planet candidate. Thus, we refer to this candidate throughout the paper as KOI-72.02.

From spectroscopy to asteroseismology, the analyses yielding fundamental stellar properties are discussed in Section 6. Section 7 contains a description of the light curve plus RV modeling that yield the planet properties of Kepler-10b (and KOI-72.02 under the planet interpretation). In the case of KOI-72.02, the absence of an RV signal implies an upper mass limit. We look for small, systematic deviations in the transit arrival times that could indicate the dynamical interaction of multiple planets orbiting Kepler-10. The implications of a null detection are discussed in Section 8. Finally, the properties of Kepler-10b are discussed in the context of the theoretical models that speak to the planet's composition. Its placement in a mass–radius diagram suggests a dry, rocky composition. Moreover, the high density ($8.8^{+2.1}_{-2.9}$ g cm^{-3}) indicates a large iron mass fraction as discussed in Section 9.

Kepler's primary objective is to determine the frequency of Earth-size planets in the habitable zone. The number of planet candidates identified in <1 year of photometry is fast approaching the thousands. Time on the large telescopes required for precision Doppler measurements is not only costly, it is insufficient for confirming Earth-size planets in the habitable zone of Sun-like stars. Instruments are not yet capable of yielding the cm s^{-1} precision required for confirmation of *Kepler's* most interesting candidates. For the near-term future, the team will focus its efforts on quantifying the false-positive rate well enough that it might be applied to the collective sample of planet candidates. The observations of Kepler-10 are part of that effort. The discovery of Kepler-10b marks an important milestone for the team: *Kepler's* first rocky planet and the smallest transiting exoplanet discovered to date.

2. *KEPLER* PHOTOMETRY

The discovery of the planet orbiting Kepler-10 begins with the high-precision *Kepler* photometry. Indeed not one but two periodic transit events were identified in the light curve, producing pipeline statistics that initiated the cascade of verification and follow-up efforts leading to confirmation and characterization of Kepler-10b.

2.1. Data Acquisition

The *Kepler* photometer is a 0.95 m effective aperture, wide field-of-view Schmidt camera in an Earth-trailing orbit. It is designed to yield 20 parts per million (ppm) relative time series precision in 6.5 hr for a 12th magnitude G2 star. The focal plane is comprised of 42 1024 × 2200 pixel science CCDs arranged together in 21 roughly square modules covering 115 deg^2 of sky (3.″98 pixel^{-1}). Each pair of CCDs forming a module shares a common sapphire field-flattener lens. The coatings deposited onto the field-flattener lenses (and, to a lesser degree, the optics and quantum efficiency of the CCDs) define the effective bandpass of the otherwise filterless photometer, yielding a mean transmission of 52.6% between 423 and 897 nm (defining the 5% transmission points). Each CCD requires its own transmission function for meaningful interpretation of color-dependent behaviors that affect planet characterization (e.g., limb darkening). A description of the instrument is given in Van Cleve & Caldwell (2009) and Argabright et al. (2008), while an overview of its in-flight performance is presented in Caldwell et al. (2010) and Jenkins et al. (2010b).

Each CCD is electronically divided into two 1024 × 1100 output units defining a total of 84 readout channels. While the photometer points at a single field continuously throughout its heliocentric orbit, it rotates about the optical axis once every ∼3 months (hereafter referred to as a quarter) in order to keep the solar panels facing the Sun. Consequently, every star spends each quarter of the year on a different channel. Kepler-10 (R.A. = 19^{h}02^{m}43.^{s}05, decl. = +50°14′28.″68) falls on channels 36 (module 11, output 4), 80 (module 23, output 4), 52 (module 15, output 4), and 8 (module 3, output 4) in quarters 0/1 (spring), 2 (summer), 3 (fall), and 4 (winter), respectively.

CCDs are read out every ∼6.5 s (6.01982 s integration and 0.51895 s read time), and every 270 readouts are co-added onboard to form 1765.5 s (∼29.4 minute) integrations (long cadence, LC). Data for up to 170,000 stars are recorded at LC, while data for up to 512 stars are also co-added to a 58.85 s (∼1 minute) integration (9 readouts) termed short cadence (SC) as described in Jenkins et al. (2010b) and Gilliland et al. (2010). The LC photometry of Kepler-10 used in the analyses reported here was acquired between 2009 May 2 and 2010 January 9—quarters 0/1 (spring) up through the first month of quarter 4 (winter). In early January, the module containing channel 8 experienced a hardware failure that was not recoverable and observations of Kepler-10 were cut short until the subsequent spacecraft roll. Over 11,000 LC observations are used in this analysis. SC data were also collected between 2009 July 21 and August 19 (one month of quarter 2) and between 2009 September 18 and 2010 January 9 (quarter 3 and the first weeks of quarter 4). The SC data were vital in determining the fundamental stellar parameters from an asteroseismic analysis (*p*-mode detection) described in Section 6.2. Approximately 200,000 SC observations were collected in this time period. Both LC and SC data are used in the light curve modeling carried out to characterize the planets. Observations of Kepler-10 continue in the three quarters each year when the target is not on the failed module.

2.2. Light Curves

Raw flux light curves are extracted by performing an unweighted sum of calibrated pixels that have been subjected to cosmic ray removal and background subtraction (Jenkins et al. 2010a). The pixels used in the sum are those defining the optimal aperture—the set of pixels that optimizes the total signal-to-noise ratio (S/N). The optimal aperture is dependent on the local pixel response function[25] (PRF), measured on-orbit during the commissioning period (Bryson et al. 2010), the distribution of stellar flux on the sky near the target (crowding), and differential velocity aberration. A complete discussion of *Kepler's*

[25] The pixel response function is a super-resolution representation of the distribution of starlight over the CCD pixels. It includes not only the effects of the instrumental optics, but also intra-pixel sensitivity and pointing jitter.

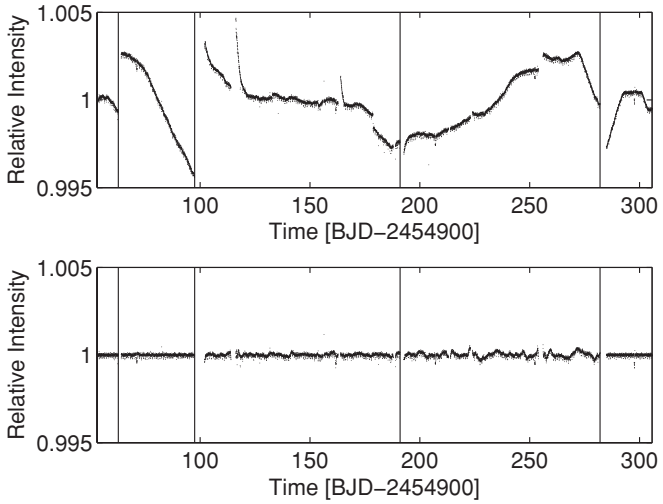

Figure 1. Raw (upper) and corrected (lower) flux time series produced by the *Kepler* photometry pipeline (PA and PDC fluxes, respectively). Vertical lines denote the boundaries between quarters. Intra-quarter flux values have been scaled by their median flux for display purpose only (to mitigate the discontinuities between quarters).

aperture photometry pipeline (PA) is given in Twicken et al. (2010a). Systematic errors, outliers, and intra-quarter discontinuities are removed by co-trending against ancillary data products in the pre-search data conditioning (PDC) pipeline module as described in Twicken et al. (2010b). Figure 1 shows the raw (upper panel) and corrected (lower panel) flux time series for Kepler-10. Vertical lines denote the boundaries between quarters. Intra-quarter fluxes were normalized by their median flux in order to reduce the magnitude of the flux discontinuities between quarters. The largest systematic errors are the long-term drifts due to image motion (differential velocity aberration) and the thermal transients after safe mode events (e.g., that near day 115). After filtering out transit events, the measured relative standard deviation of the PDC-corrected, LC light curve is 62 ppm per (LC) cadence. An expected instrument + photon noise is computed for each flux in the time series. The mean of the per (29.4 minute) cadence noise estimates reported by the pipeline is 36 ppm. Both raw (PA) and corrected (PDC) light curves are available at the Multi-Mission Archive at Space Telescope Science Institute, MAST.[26]

With regards to the time stamps associated with each photometric flux, we note that *Kepler's* fundamental coordinate system is UTC for all time tags. Spacecraft times are converted to barycentric-corrected Julian dates at the mid-time of each cadence.

2.3. Transiting Planet Search

The Kepler-10b transits were identified by the transiting planet search (TPS) pipeline module that searches through each systematic error-corrected flux time series for periodic sequences of negative pulses corresponding to transit signatures. The approach is a wavelet-based, adaptive matched filter that characterizes the power spectral density of the background process (i.e., anything that is not related to the transit signal itself, such as stellar variability, instrumental signatures, differential velocity aberration-induced photometric drift, etc.) yielding the observed light curve and uses this time-variable power spectral density estimate to realize a pre-whitening filter to apply to the light curve (Jenkins et al. 2010d). TPS then convolves a transit waveform, whitened by the same pre-whitening filter as the data, with the whitened data to obtain a time series of single-event statistics. These represent the likelihood that a transit of that duration is present at each time step. The single-event statistics are then combined into multiple-event statistics by folding them at trial orbital periods ranging from 0.5 days to as long as one quarter (∼90 days). The step sizes in period and epoch are chosen to control the minimum correlation coefficient between neighboring transit models used in the search so as to maintain a high sensitivity to transit sequences in the data.

KOI-72.01 was identified by TPS in each quarter of data with a multiple event statistic $>15\sigma$. The long-period transits of KOI-72.02 were identified by manual inspection due to the fact that the current version of TPS does not operate on more than one quarter of data at a time making detection of events with periods beyond ∼30 days necessarily incomplete. Multi-quarter functionality is slated for the next software release in early 2011. The transit depth, duration, period, and epoch are derived from physical modeling (see Section 7) using all of the available data. KOI-72.01 is characterized as a 152 ± 4 ppm dimming lasting 1.811 ± 0.024 hr with transit ephemeris of T [BJD] $= 2454964.57375^{+0.00060}_{-0.00082} + N*0.837495^{+0.000004}_{-0.000005}$ days. KOI-72.02 is characterized as a 376 ± 9 ppm dimming lasting 6.86 ± 0.07 hr and an ephemeris T [BJD] $= 2454971.6761^{+0.0020}_{-0.0023} + N * 45.29485^{+0.00065}_{-0.00076}$ days.

3. DATA VALIDATION

Astrophysical signals mimicking planet transits are routinely picked up by the pipeline. The large majority of such false positives can be identified via statistical tests performed on the *Kepler* data itself—tests that are collectively referred to as data validation. Data validation for *Kepler's* first planet discoveries (Kepler-4b, 5b, 6b, 7b, and 8b) is described in Batalha et al. (2010b). These are gradually being replaced by pipeline software products such as those described in Wu et al. (2010). Only targets passing each of these statistical tests are passed on to the Follow-up Observation Program team for further vetting, confirmation, and characterization. It is at this stage that stars are assigned a "*Kepler* object of interest" number. Kepler-10 was referred to as KOI-72 throughout the vetting stages. More specifically, the short-period event was referred to as KOI-72.01 while the long-period event was referred to as KOI-72.02. We will use these identifiers in the subsequent discussions of the analyses that led to confirmation. Here we describe the data validation metrics—statistics which, taken alone, support the planet interpretation for both KOI-72.01 and KOI-72.02.

3.1. Binarity Tests

For each event, the even-numbered transits and odd-numbered transits are modeled independently using the techniques described in Section 7. The depth of the phase-folded even-numbered transits is compared to that of the odd-numbered transits as described in Batalha et al. (2010b). A statistically significant difference in the transit depths is an indication of a diluted or grazing eclipsing binary system. Neither of the transit events detected in the light curve of Kepler-10 shows odd–even depth differences outside of 2σ, where σ refers to the uncertainty in the transit depths reported in Section 2.3 (6 and 9 ppm for KOI-72.01 and KOI-72.02, respectively).

[26] http://archive.stsci.edu/kepler

Table 1
Observed Flux-weighted Centroid Shifts for KOI-72.01

Metric	Q1	Q2	Q3
ΔR	$6.07 \times 10^{-5} \pm 2.42 \times 10^{-5}$	$7.36 \times 10^{-6} \pm 2.40 \times 10^{-5}$	$-4.91 \times 10^{-7} \pm 2.42 \times 10^{-5}$
ΔC	$6.96 \times 10^{-5} \pm 1.59 \times 10^{-5}$	$-1.12 \times 10^{-5} \pm 1.25 \times 10^{-5}$	$-8.75 \times 10^{-6} \pm 1.59 \times 10^{-5}$
D	$9.23 \times 10^{-5} \pm 1.99 \times 10^{-5}$	$1.34 \times 10^{-5} \pm 9.25 \times 10^{-5}$	$8.77 \times 10^{-6} \pm 1.59 \times 10^{-5}$
D/σ	4.64	0.79	0.55

The modeling allows for the presence of a secondary eclipse (or occultation event) near phase = 0.5 and reports the significance of such a signal. While its presence does not rule out the planetary interpretation, it acts as a flag for further investigation. More specifically, the flux decrease is translated into a surface temperature assuming a thermally radiating disk, and this temperature is compared to the equilibrium temperature of a low albedo (0.1) planet at the modeled distance from the parent star. There is a marginal detection ($\sim 2\sigma$) of a secondary eclipse associated with KOI-72.01. At just 6 ppm (see Table 7), the flux change is not severe enough to rule out the planetary interpretation (i.e., that it is due to an occultation of a planetary companion). There is no detection of a secondary eclipse associated with KOI-72.02. The binarity tests are consistent with the planet interpretation for both transit events in the light curve of Kepler-10.

3.2. Photocenter Tests

To check for false positives due to background eclipsing binaries, we study the behavior of flux centroids—the center-of-light distribution in the photometric aperture—and how it behaves as a function of time, especially comparing images taken during transits with those taken outside of transit. We rely primarily on flux-weighted centroids and modeling the expected behavior based on the local distribution of point sources from the *Kepler* Input Catalog (KIC) and supplemented by high spatial resolution imaging (Section 4.2). Neither speckle nor AO imaging reveal any point sources in the photometric aperture that were not already listed in the KIC.

The study of centroid behavior is complicated by the fact that the Kepler-10 image is saturated in all quarters. In quarter 2, the star is on the edge of saturation, but it is apparent that there is some spilling of charge even in this case. Saturation behavior on the *Kepler* focal plane is known to be conservative (e.g., all charge is captured) but has strong pixel-to-pixel variation in details such as saturation level and the fraction of flux that spills up and down the CCD columns.

The high-accuracy technique of fitting the PRF to the difference image formed by subtracting the in-transit image from the out-of-transit image is inappropriate for saturated targets, because the saturated pixels do not represent the PRF of the star, and such mismatches between the pixel data and the PRF cause significant position biases in the PRF fit. As an alternative, we use a modified PRF fit technique, described below.

We compute flux-weighted centroids by creating out-of-transit and in-transit images from detrended, folded pixel time series. Separate images are created for KOI-72.01 and KOI-72.02. For each pixel time series, the de-trending operation has three steps: (1) removal of a median filtered time series with a window size equal to the larger of 48 cadences or three times the transit duration, (2) removal of a robust low-order polynomial fit, and (3) the application of a Savitzky-Golay filtered time series of order three with a width of 10 cadences (5 hr). The Savitzky-Golay filter is not applied within two cadences of a transit event, so the transits are preserved. The resulting pixel time series are folded by the transit period. Each pixel in the out-of-transit image is the average of 30 points taken from the folded time series outside the transit, 15 points on each side of the transit event. Each pixel in the in-transit image is the average of as many points in the transit as possible: three for KOI-72.01 and eleven for KOI-72.02. In the former case, though there are fewer points per transit, there are significantly more transits to draw from (several hundred for KOI-72.01 compared to just six for KOI-72.02). Consequently, KOI-72.01 yields smaller uncertainties.

A flux-weighted centroid is computed for the out-of-transit image and the in-transit-image using all of the pixels in the mask[27] of Kepler-10. This produces row and column centroid offsets ΔR and ΔC, and the centroid offset distance $D = \sqrt{\Delta R^2 + \Delta C^2}$.

Uncertainties of these centroids are estimated via Monte Carlo simulation, where a noise realization is injected into 48 cadence smoothed versions of the pixel time series for each trial. A total of 2000 trials are performed each for KOI-72.01 and KOI-72.02. The in- and out-of-transit images are formed using the same detrending, folding, and averaging as the flight data. The measured uncertainties are in the range of a few times 10^{-5} pixels.

Table 1 shows the resulting measurements of the KOI-72.01 centroids from quarter 1, 2, 3, and 4 pixel data, along with the Monte Carlo based 1σ uncertainties. The centroids are converted into centroid offsets and offset distance with propagated uncertainties. We see that while in quarter 1 there is a $>4\sigma$ observed offset, in quarters 2 and 3 the observed offset is less than 1σ. Quarter 1 had significant thermal and pointing systematics, while quarter 2 had significant pointing drift. These systematics were significantly reduced by quarter 3.

Table 2 shows the measured centroid shifts and uncertainties for KOI-72.02 in quarters 1–4. The KOI-72.02 transit uncertainties in quarter 3 are smaller because only one transit was observed in quarters 1, 2, and 4, while two transits were observed in quarter 3. Generally, the centroid shifts for KOI-72.02 are larger than KOI-72.01. This larger centroid shift may be indicative of the KOI-72.02 transit event being due to a background eclipsing binary, or the larger shift may be due to the deeper transits of KOI-72.02 (larger flux changes induce larger centroid shifts) combined with the complex behavior of pixels at or near saturation. To study this question PRF-fit centroids that ignore saturated pixels are computed for the KOI-72.02 in- and out-of-transit images, and the resulting centroid shifts are computed. These results are shown in Table 3. This technique indicates no statistically detectable centroid motion in quarter 3. The uncertainties were computed via Monte Carlo methods similar to those used to compute the flux-weighted centroid uncertainties.

[27] Each star observed by *Kepler* has a predefined mask that defines the pixel set that is downloaded from the spacecraft. The mask changes from quarter to quarter since the star falls on a different CCD channel upon quarterly spacecraft rotation.

Table 2
Observed Flux-weighted Centroid Shifts for KOI-72.02

Metric	Q1	Q2	Q3
ΔR	$2.70 \times 10^{-4} \pm 4.08 \times 10^{-5}$	$-1.90 \times 10^{-4} \pm 5.35 \times 10^{-5}$	$3.14 \times 10^{-5} \pm 3.05 \times 10^{-5}$
ΔC	$7.58 \times 10^{-5} \pm 2.87 \times 10^{-5}$	$1.91 \times 10^{-4} \pm 4.03 \times 10^{-5}$	$-3.84 \times 10^{-5} \pm 2.45 \times 10^{-5}$
D	$2.81 \times 10^{-4} \pm 4.01 \times 10^{-5}$	$2.69 \times 10^{-4} \pm 4.73 \times 10^{-5}$	$4.96 \times 10^{-5} \pm 2.70 \times 10^{-5}$
D/σ	7.01	5.68	1.83

Table 3
PRF-fit Centroid Shifts for KOI-72.02 Without Saturated Pixels

Metric	Q1	Q2	Q3
ΔR	$3.05 \times 10^{-4} \pm 7 \times 10^{-5}$	$-1.82 \times 10^{-4} \pm 7 \times 10^{-5}$	$5.50 \times 10^{-5} \pm 7 \times 10^{-5}$
ΔC	$1.72 \times 10^{-4} \pm 7 \times 10^{-5}$	$-1.84 \times 10^{-4} \pm 7 \times 10^{-5}$	$4.39 \times 10^{-5} \pm 7 \times 10^{-5}$
D	$3.50 \times 10^{-4} \pm 7 \times 10^{-5}$	$2.59 \times 10^{-4} \pm 7 \times 10^{-5}$	$7.05 \times 10^{-5} \pm 7 \times 10^{-5}$
D/σ	4.9	3.7	1.0

Table 4
Modeled Centroid Shifts Due to Transits on the Known Stars in the Q3 Aperture with Depths that Reproduce the Observed Q3 Depth

Object	Modeled Depth	Modeled D	D/σ	Object	Modeled Depth	Modeled D	D/σ
KOI-72.01	1.67×10^{-4}	6.10×10^{-6}	0.384	KOI-72.02	5.52×10^{-4}	2.02×10^{-5}	0.747
11904143	1.90×10^{-1}	5.69×10^{-4}	35.8	11904143	6.30×10^{-1}	1.89×10^{-3}	69.7
11904165	6.31×10^{-2}	3.53×10^{-4}	22.2	11904165	2.09×10^{-1}	1.17×10^{-3}	43.3
11904167	1.17×10^{-1}	4.43×10^{-4}	27.9	11904167	3.88×10^{-1}	1.47×10^{-3}	54.3
11904169	7.13×10^{-1}	6.73×10^{-4}	42.3	11904169	2.36	...	...
11904171	2.22×10^{-1}	6.94×10^{-4}	43.6	11904171	7.35×10^{-1}	2.30×10^{-3}	84.9
11904145	1.55×10^{-1}	4.04×10^{-4}	25.4	11904145	5.13×10^{-1}	1.34×10^{-3}	49.5
11904150	1.10	...	...	11904150	3.63	...	...
11904152	1.95×10^{-1}	5.46×10^{-4}	34.3	11904152	6.46×10^{-1}	1.81×10^{-3}	66.8
11904154	3.08×10^{-1}	6.51×10^{-4}	40.9	11904154	1.02	...	...
11904155	1.56	...	...	11904155	5.15	...	...
11904158	3.09×10^{-2}	6.53×10^{-4}	41.1	11904158	1.02×10^{-1}	2.16×10^{-3}	80.0
11904159	1.16×10^{-1}	5.63×10^{-4}	35.4	11904159	3.82×10^{-1}	1.86×10^{-3}	69.0
11904160	2.51×10^{-2}	2.04×10^{-4}	12.8	11904160	8.31×10^{-2}	6.74×10^{-4}	24.9
11904162	1.06×10^{-1}	4.09×10^{-4}	25.7	11904162	35.1×10^{-1}	1.35×10^{-3}	50.1

Note. Transits on some companions can be ruled out because they require depth >1.

While both the flux-weighted centroid and PRF fitting methods indicate statistically significant centroid motion on KOI-72.02 in quarters 1, 2, and 4, we point out that the directions of the centroid offsets are inconsistent from quarter to quarter. This indicates that these centroid offsets are not likely to be due to a background object in the sky.

The observed centroids are compared with the modeled centroids computed using point sources cataloged in the KIC (Latham et al. 2005) out to 15 pixels beyond the mask. As described in Sections 4.2.1 and 4.2.2, no additional point sources were identified in speckle or AO imaging. To generate the modeled out-of-transit image, the measured PRF is placed at each star's location on the focal plane, scaled by that star's flux. This provides the contribution of each star to the flux in the mask. For each star s_i in the mask, the depth d_{s_i} of a transit is computed that reproduces the observed depth in the individual pixels. An in-transit image for each s_i is similarly but with s_i's flux suppressed by $1 - d_{s_i}$. These model images are subject to errors in the PRF (Bryson et al. 2010), so they will not exactly match the sky. Further, a very simple saturation model is applied which spills saturation symmetrically up and down the column.

The modeled centroids (using the quarter 3 mask definition) are presented in Table 4. For both KOI-72.01 and KOI-72.02 the offset expected for a transit associated with Kepler-10 (and not a nearby star) is smaller than the 1σ uncertainties in D computed from the flux-weighted centroid measurements. Modeled transits on other stars in the mask predict centroid shift in excess of 10σ, which would be readily observed in our flux-weighted centroids. We can therefore rule out all known stars in the mask as responsible for the transit signal on both KOI-72.01 and KOI-72.02.

There is a radius beyond which any star capable of producing the observed transit signal would also induce a centroid shift large enough to be detected in the *Kepler* data when comparing in- and out-of-transit images. We estimate this confusion radius by scaling the 3σ centroid offset uncertainty by the observed transit depth as described in Section 4.1.3 of Wu et al. (2010). For this, we use the quarter 3 uncertainty in D. This radius of confusion for KOI-72.01 is 1.17 arcsec, and the radius of confusion for KOI-72.02 is 0.60 arcsec. The volume subtended by this area on the sky can be used in a BLENDER analysis (Section 5) to assess the probability of encountering an eclipsing binary (capable of producing the transit signal) in that volume of the Galaxy. However, in the case of Kepler-10 the high spatial resolution imaging described in Sections 4.2.1 and 4.2.2 provides tighter constraints on the background star population.

4. FOLLOW-UP OBSERVATIONS

Each of the periodic transit signals identified in the light curve of Kepler-10 passes all of the data validation tests that might indicate the possibility of a false positive as described

in Section 3. The star was passed to the follow-up observing team on 2009 July 21 after identification and scrutiny of the short-period transit event (KOI-72.01). This initiated a series of ground-based observations that began with reconnaissance spectroscopy to confirm the stellar parameters in the KIC and identify any obvious eclipsing binary signatures (Section 4.1), continued with high spatial resolution imaging to identify nearby stars in the photometric aperture (Section 4.2), and ended with high-resolution, high S/N echelle spectroscopy with and without an iodine cell to compute stellar parameters, probe magnetic activity, measure line bisectors, and make precision Doppler measurements. The follow-up observations do not rule out the planetary interpretation for either of the transit signatures. However, they only allow for the confirmation and characterization of the short-period candidate, KOI-72.01, as discussed in Section 4.3.

4.1. Reconnaissance Spectroscopy

Spectroscopic observations on medium-class telescopes are acquired before requesting precision Doppler measurements. These "reconnaissance" spectra are used to improve upon the photometrically derived stellar classification from the KIC ($T_{\rm eff}$ = 5491 K, $\log g$ = 4.47, $R_\star$ = 0.983 $R_\odot$), identify double-lined spectroscopic binaries, and search for indications of RV variations larger than $\sim$1 km s^{-1} that might suggest a stellar companion. The objective is continued false-positive elimination.

Two reconnaissance spectra were obtained with the Hamilton echelle on the Shane 3 m telescope at the Lick Observatory. High S/N observations were acquired on two successive nights in 2009 August, at heliocentric Julian dates 2455046.771 and 2455047.758, corresponding to phases 0.146 and 0.3251 for KOI-72.01, and to phases 0.658 and 0.680 for KOI-72.02. The spectral order covering about 7.0 nm centered on the Mg b lines was correlated against a library of synthetic spectra calculated by John Laird using a line list prepared by Jon Morse. The stellar parameters for the template spectrum that yielded the highest value for the peak correlation coefficient were $T_{\rm eff} = 5750 \pm 125$ K, $\log g = 4.5 \pm 0.25$, and $v \sin i = 0.0^{+2}_{-0}$ km s^{-1} for an assumed solar metallicity. The errors quoted for $T_{\rm eff}$ and $\log g$ are half the spacing of the library grid. The two Lick exposures were unusually high S/N compared to typical reconnaissance spectra, with a peak value for the correlation coefficient of 0.98. Consequently, we were able to estimate the metallicity and to interpolate to finer values of the temperature and gravity, obtaining $T_{\rm eff} = 5680 \pm 91$ K, $\log g = 4.33 \pm 0.16$, and [Fe/H] = -0.09 ± 0.04. The correlation functions for the two Lick observations showed no evidence of a composite spectrum, and the two velocities agreed within 0.1 km s^{-1}. Thus, there was no suggestion of a stellar companion responsible for either system of transit events, and the reconnaissance spectroscopy confirms that Kepler-10 is a Sun-like, slowly rotating main-sequence star, and supports the planetary interpretation for the transit events. Consequently, the star was scheduled for precision Doppler measurements (see Section 4.3).

4.2. High Spatial Resolution Imaging

The more complete our knowledge of stellar flux sources in the photometric aperture, the better we are able to assess the likelihood of a blend scenario in the interpretation of the transit event. Much of this knowledge comes from the KIC which federates point sources from the USNO-B catalog, the 2MASS catalog, and our own pre-launch Stellar Classification Program. Identification of point sources within a 1.″5 radius requires additional imaging.

4.2.1. Speckle Imaging

Speckle imaging of Kepler-10 was obtained on the night of 2010 June 18 UT using the two-color speckle camera at the WIYN 3.5 m telescope located on Kitt Peak. The speckle camera simultaneously obtained 2000 30 ms EMCCD images in two filters: V (5620/400 Å) and R (6920/400 Å). These data were reduced and processed to produce a final reconstructed speckle image for each filter. Figure 2 shows the reconstructed R-band image. North is up and east is to the left in the image and the "cross" pattern seen in the image is an artifact of the reconstruction process. The details of the two-color EMCCD speckle camera are presented in S. B. Howell et al. (2011, in preparation).

For the speckle data, we determine if a companion star exists within the approximately 2.5 × 2.5 arcsec box centered on the target and robustly estimate the background limit we reach in each summed, reconstructed speckle image. The two-color system allows us to believe single fringe detection (finding and modeling identical fringes in both filters) if they exist and rule out companions between 0.05 arcsec and 1.5 arcsec from Kepler-10. The speckle image was obtained with the WIYN telescope native seeing near 0.7 arcsec, and we find no Kepler-10 companion star within the speckle image separation detection limits to a magnitude limit of 6 mag in R and 4.5 mag in V below the brightness of Kepler-10.

4.2.2. AO Imaging

Near-infrared adaptive optics imaging of KOI-72 was obtained on the night of 2009 September 8 UT with the Palomar Hale 200″ telescope and the PHARO near-infrared camera (Hayward et al. 2001) behind the Palomar adaptive optics system (Troy et al. 2000). PHARO, a 1024 × 1024 HgCdTe infrared array, was utilized in 25.1 mas pixel^{-1} mode yielding a field of view of 25 arcsec. Observations were performed using a J filter (λ_0 = 1.25 μm). The data were collected in a standard five-point quincunx dither pattern (e.g., dice pattern for number five) of 5 arcsec steps interlaced with an off-source (60 arcsec east) sky dither pattern. Data were taken at two separate times within the same night—150 frames using 1.4 s integration times and 150 frames using 2.8 s integration times—for a total on-source integration time of 10 minutes. The individual frames were reduced with a custom set of IDL routines written for the PHARO camera and were combined into a single final image. The adaptive optics system guided on the primary target itself and produced measured Strehl ratios of 0.15 at J with a central core width of FWHM = 0.075 arcsec. The final co-added image at J is shown in Figure 3.

No additional sources were detected at J within 6.25 arcsec of the primary target. Source detection completeness was accomplished by randomly inserting fake sources of various magnitudes in steps of 0.5 mag and at varying distances in steps of 1.0 FWHM from the primary target. Identification of sources was performed both automatically with the IDL version of DAOPhot and by eye. Magnitude detection limits were set when a source was not detected by the automated FIND routine or by eye. Within a distance of 1–2 FWHM, the automated finding routine often fails even though the eye can discern two sources. Beyond that distance the two methods agreed well. A

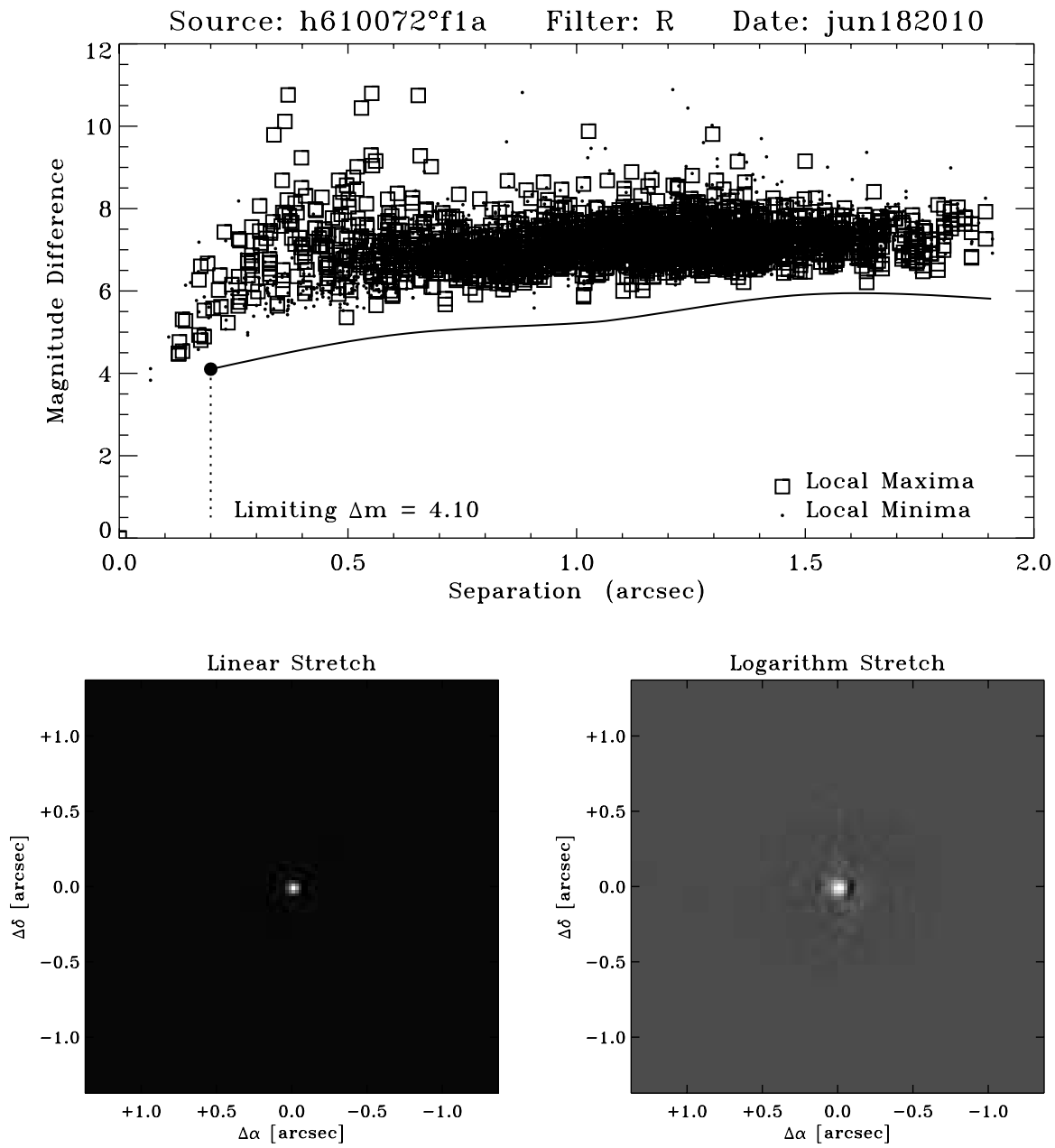

Figure 2. Speckle reconstructed *R*-band image of Kepler-10. No other source is observed to within 1.8 arcsec of the target to a depth of ∼6 mag. The cross pattern is an artifact of the reconstruction process. North/east are up/left.

summary of the detection efficiency as a function of distance from the primary star is given in Table 5.

4.3. Precise Doppler Measurements of Kepler-10

We obtained 40 high-resolution spectra of Kepler-10 between 2009 August 31 and 2010 August 6 using the HIRES spectrometer on the Keck I 10 m telescope (Vogt et al. 1994). We used the same configuration of HIRES that is normally used for precise Doppler work of nearby FGK stars (Marcy et al. 2008) which yields a Doppler precision of 1.0–1.5 m s^{-1} depending on spectral type and rotational $v \sin i$. The HIRES fiber feed was not used for these observations. The standard iodine cell was placed in the telescope beam to superimpose iodine lines directly on the stellar spectrum. As the iodine lines and stellar lines are carried by exactly the same photons hitting the same optics, both sets of lines share precisely the same instrumental

Table 5
Palomar AO Source Sensitivity as a Function of Distance from the Primary Target at *J*

Distance (FWHM)	Distance (arcsec)	Δ*J* (mag)	*J* (mag)
1	0.075	1.5	11.4
2	0.150	3.5	13.4
3	0.225	5.0	14.9
4	0.300	5.0	14.9
5	0.375	5.5	15.4
6	0.450	5.5	15.4
7	0.525	6.5	16.4
8	0.600	7.0	16.9
9	0.675	7.5	17.4
40	3.000	9.5	19.4

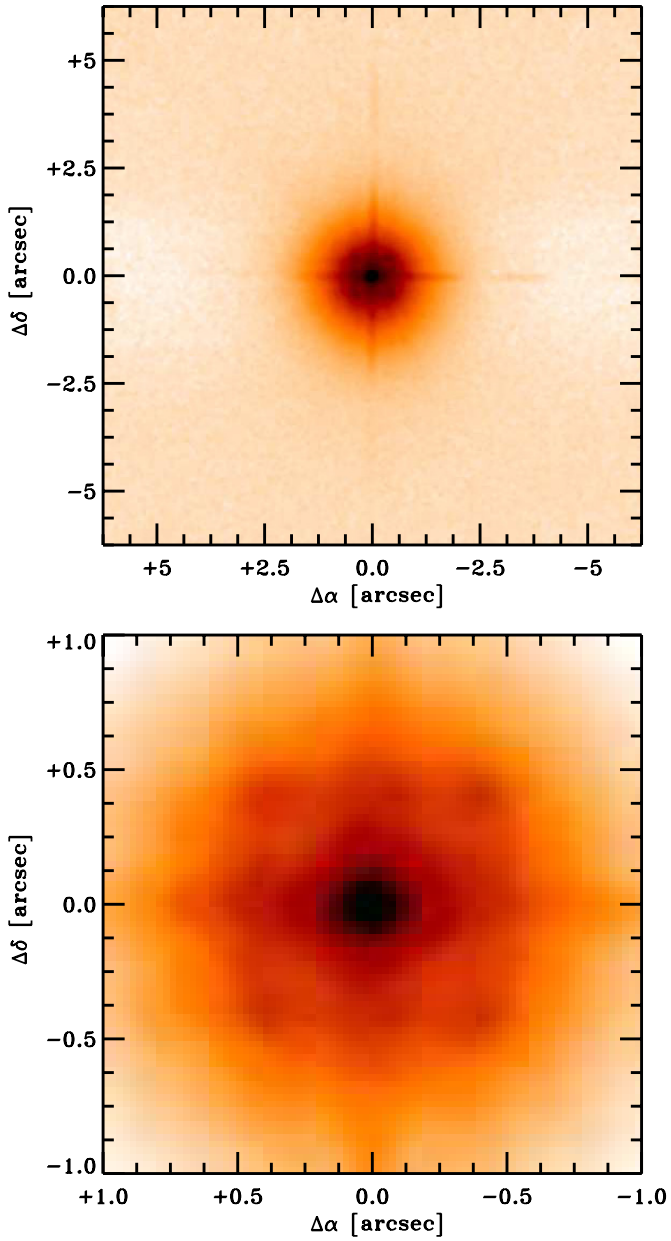

Figure 3. *J*-band Palomar adaptive optics image of KOI-72. The top image displays a 12.″5 × 12.″5 field of view centered on the primary target. The bottom image displays a 2″ × 2″ field of view centered on the primary target. The four-point pattern surrounding the central point-spread function core is part of the adaptive optics point-spread function.

(A color version of this figure is available in the online journal.)

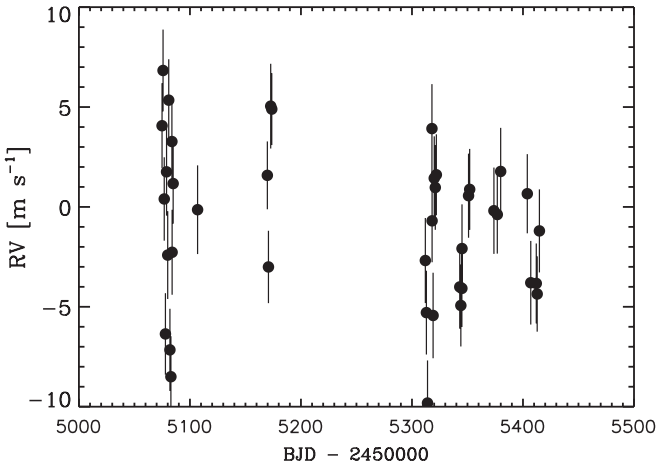

Figure 4. Radial velocities derived from HIRES spectra collected in 2009 and 2010 are plotted against time. Error bars include not only the expected instrumental noise but also a 2 m s^{-1} jitter to account for variations intrinsic to the star.

profile and wavelength scale. The iodine lines represent exactly the same spectrometer optics as the stellar spectrum, with no difference. We fit the composite spectrum of iodine and stellar lines simultaneously in each 100 pixel segment of spectrum, yielding a Doppler shift that automatically includes the instantaneous wavelength scale and instrumental profile. This dual fitting limits the long-term and short-term systematic Doppler errors at ∼1.0 m s^{-1}.

Most observations were made with the "C2 decker" entrance aperture which projects to 0.″87 × 14.″0 on the sky, giving a resolving power of about 60,000 at 5500 Å and enabling sky subtraction (typical seeing is 0.″6–1.″2). A few observations were made with the B5 decker 0.″87 × 3.″0 that does not permit sky subtraction. It is possible that a few of those observations suffered from minor moonlight contamination. The average exposure was 30 minutes, with some as short as 15 minutes and others as 45 minutes, depending on seeing and clouds.

The raw CCD images were reduced by subtracting an average bias, subtracting the sky counts at each wavelength just above and below the stellar spectrum, flat-fielding the spectrum with a 48 exposure sum from a quartz lamp, and extracting the spectrum with a width that includes 99.99% of the spectrum. Cosmic rays were removed from the raw image first. The pixels typically contained approximately 20,000 photons giving a Poisson-limited S/N of 140. We performed the Doppler analysis with the algorithm of Johnson et al. (2009). The internal Doppler errors (the weighted uncertainty in the mean of 400 spectral segments) are typically 1.5–2.0 m s^{-1}. The resulting velocities are given in Table 6 and shown in Figure 4 as a function of time. The error bars include the internal Doppler errors and an assumed jitter of 2 m s^{-1} (see below), added in quadrature. The center-of-mass velocity relative to the solar system barycenter (Gamma Velocity) for Kepler-10 is −98.93 ± 0.02 km s^{-1} (Table 7). This is an unusually large RV, indicative of old disk or even halo membership. The low metallicity (Section 6.1), [Fe/H] = −0.15 ± 0.04, magnetic activity (Section 6.1), and asteroseismic age, 11.9 ± 4.5 Gyr (Section 6.2) also suggest old disk or halo membership.

Nearby stars with $T_{\rm eff}$ near 5600 K and log g near 4.35 such as KOI-72 have been previously surveyed for precise Doppler work, revealing a noise-like "jitter" of ∼2.5 m s^{-1} caused by surface effects including turbulence, spots on the rotating star, acoustic oscillations, and atmospheric flows associated with magnetic flux tubes. While each effect has its own time scale, it is practical to account for jitter by simply adding it in quadrature to the internal errors to yield an estimate of the total uncertainty in the star's velocity. We have included a jitter of 2.0 m s^{-1} in the model fit to all of the data, photometric, and velocities.

A periodogram (Figure 5) of the velocities exhibits a tall peak at a period of 0.837 day, in agreement with the photometric period of the KOI-72.01. The coincidence between the transit and RV periods to three significant digits suggests that the RV period is physically related to the transits, as expected if the RV periodicity stems from the reflex motion of the star in response to the gravitational influence of the planet. The periodogram also shows a peak at a period near 1.2 days, which is the

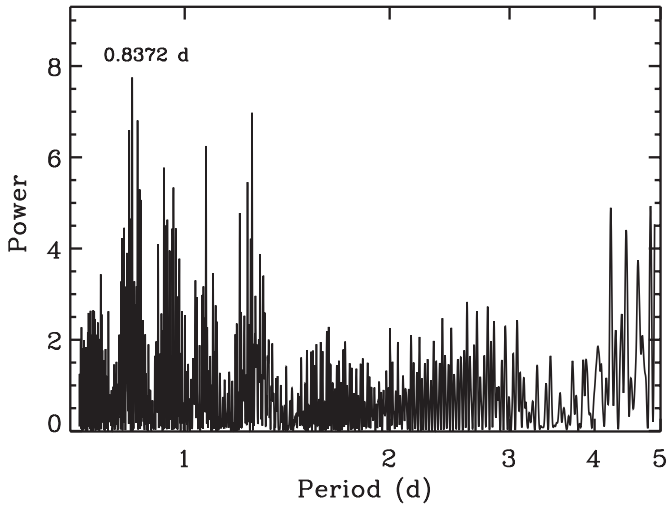

Figure 5. Periodogram of the radial velocities shows a peak in the spectral density at the photometric period derived from the transits of Kepler-10b.

Table 6
Relative Radial Velocity Measurements of KOI-72

HJD (−2450000)	RV (m s^{-1})	σ_{RV} (m s^{-1})
5074.878	4.06	1.6
5075.773	6.83	1.5
5076.863	0.40	1.5
5077.923	−6.36	1.5
5078.922	1.76	1.7
5079.973	−2.41	1.7
5080.896	5.34	1.5
5081.969	−7.16	1.5
5082.848	−8.50	1.5
5083.761	3.27	1.4
5083.945	−2.27	1.6
5084.878	1.17	1.4
5106.890	−0.14	1.7
5169.725	1.58	0.9
5170.725	−3.00	1.1
5172.756	5.05	1.6
5173.721	4.90	1.1
5312.047	−2.68	1.6
5313.004	−5.29	1.5
5314.005	−9.82	1.6
5317.998	3.92	1.7
5318.121	−0.70	1.5
5319.027	−5.43	1.6
5320.063	1.44	1.5
5321.007	0.97	1.6
5321.969	1.61	1.5
5343.050	−4.01	1.5
5344.032	−4.93	1.5
5344.973	−4.08	1.3
5345.068	−2.08	1.7
5350.973	0.56	1.6
5351.988	0.88	1.4
5373.814	−0.19	1.6
5376.865	−0.38	1.4
5379.902	1.78	1.7
5403.898	0.66	1.4
5407.013	−3.80	1.5
5411.986	−3.83	1.4
5412.805	−4.36	1.2
5414.803	−1.20	1.5

Table 7
Star and Planet Parameters for the Kepler-10 System

Parameter	Value	Notes
Transit and orbital parameters: Kepler-10b		
Orbital period, P (days)	$0.837495^{+0.000004}_{-0.000005}$	A
Midtransit time, E (BJD)	$2454964.57375^{+0.00060}_{-0.00082}$	A
Scaled semimajor axis, $a/R_\star$	$3.436^{+0.070}_{-0.092}$	A
Scaled planet radius, $R_P/R_\star$	$0.01232^{+0.00013}_{-0.00016}$	A
Impact parameter, b	$0.339^{+0.073}_{-0.079}$	A
Orbital inclination, i (deg)	$84.4^{\circ}0^{+1.1}_{-1.6}$	A
Orbital semi-amplitude, K (m s^{-1})	$3.3^{+0.8}_{-1.0}$	B
Orbital eccentricity, e	0	B
Center-of-mass velocity, γ (m s^{-1})	-98.93 ± 0.02	B
Transit and orbital parameters: KOI-72.02		
Orbital period, P (days)	$45.29485^{+0.00065}_{-0.00076}$	A
Midtransit time, E (HJD)	$2454971.6761^{+0.0020}_{-0.0023}$	A
Scaled semimajor axis, $a/R_\star$	$49.1^{+1.2}_{-1.3}$	A
Scaled planet radius, $R_P/R_\star$	$0.019378^{+0.00020}_{-0.00024}$	A
Impact parameter, b	$0.299^{+0.089}_{-0.073}$	A
Orbital inclination, i (deg)	$89.7^{\circ}0^{+0.09}_{-0.12}$	A
Observed stellar parameters		
Effective temperature, $T_{\rm eff}$(K)	5627 ± 44	C
Spectroscopic gravity, log g(cgs)	4.35 ± 0.06	C
Metallicity, [Fe/H]	-0.15 ± 0.04	C
Projected rotation, $v \sin i$(km s^{-1})	0.5 ± 0.5	C
Fundamental Stellar Properties		
Mass, $M_\star(M_\odot)$	0.895 ± 0.060	D
Radius, $R_\star(R_\odot)$	1.056 ± 0.021	D
Surface gravity, log $g_\star$ (cgs)	4.341 ± 0.012	D
Luminosity, $L_\star$ ($L_\odot$)	1.004 ± 0.059	D
Absolute V magnitude, M_V (mag)	4.746 ± 0.063	D
Age (Gyr)	11.9 ± 4.5	D
Distance (pc)	173 ± 27	D
Planetary parameters: Kepler-10b		
Mass, M_P ($M_\oplus$)	$4.56^{+1.17}_{-1.29}$	A, B, C, D
Radius, R_P ($R_\oplus$)	$1.416^{+0.033}_{-0.036}$	A, B, C, D
Density, ρ_P (g cm^{-3})	$8.8^{+2.1}_{-2.9}$	A, B, C, D
Surface gravity, log g_P (cgs)	$3.35^{+0.11}_{-0.13}$	A, B, C, D
Orbital semimajor axis, a (AU)	$0.01684^{+0.00032}_{-0.00034}$	E
Equilibrium temperature, $T_{\rm eq}$ (K)	1833	F
Parameters for candidate: KOI-72.02		
Mass, M_P ($M_\oplus$)	<20	G
Radius, R_P ($R_\oplus$)	$2.227^{+0.052}_{-0.057}$	A, D
Orbital semimajor axis, a (AU)	$0.2407^{+0.0044}_{-0.0053}$	E
Equilibrium temperature, $T_{\rm eq}$ (K)	485	F

Notes. A: based primarily on an analysis of the photometry, B: based on a joint analysis of the photometry and radial velocities, C: based on an analysis by D. Fischer of the Keck/HIRES template spectrum using SME (Valenti & Piskunov 1996), D: based on asteroseismology analysis E: based on Newton's revised version of Kepler's Third Law and the results from D, F: calculated assuming a Bond albedo of 0.1 and complete redistribution of heat for reradiation, and G: upper limit corresponding to three times the 68.3% credible interval from MCMC mass distribution.

alias resulting from the nightly observational cadence. Similarly, there is another peak near a period of 5 days (off the figure) that is the alias caused by the beating of the 0.827 day period with the 1.0 day cadence of observations. There is no indication of power at the period of KOI-72.02.

The velocities phased to the photometric period of KOI-72.01 (Figure 6) show a clear, continuous, and nearly sinusoidal variation consistent with a nearly circular orbit of a planetary

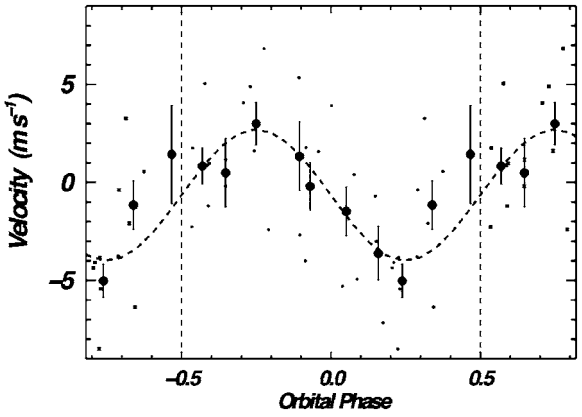

Figure 6. Radial velocities vs. phase derived from transit photometry of the short-period event. Both individual velocities are plotted (small circles) as well as averages over 0.1 phase bins (large circles). The dashed line shows the best-fit circular orbit solution for which there are only two free parameters—the amplitude K and the zeropoint of the velocities.

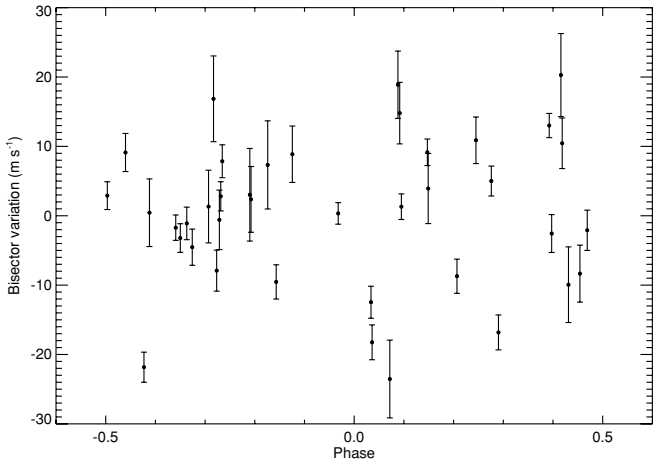

Figure 7. Line bisector span measurements folded at the photometric period.

companion. The lack of any discontinuities in the phased velocity plot argues against a background eclipsing binary star as the explanation. Such a binary with a period of 0.83 day would have orbital semi-amplitudes of hundreds of kilometers per seconds, so large that the spectral lines would completely separate from each other, and separate from the lines of the main star. Such breaks in the spectral-line blends would cause discontinuities in the velocity variation, which is not seen here. Thus, the chance that the 0.83 day periodicity exhibited independently in both the photometry and velocities might be caused by an eclipsing binary seems quite remote.

Precision Doppler measurements are used to constrain the mass of KOI-72.01 (Kepler-10b) as discussed in Section 7. The absence of a Doppler signal for KOI-72.02 is used to compute an upper limit to the mass of this candidate under the planet interpretation.

4.4. Bisector Analysis

From the Keck spectra, we computed a mean line profile and the corresponding mean line bisector. Time-varying line asymmetries are tracked by measuring the bisector spans—the velocity difference between the top and bottom of the mean line bisector—for each spectrum (Torres et al. 2005). When RV variations are the result of a blended spectrum between a star and an eclipsing binary, we expect the bisectors to reveal a phase-modulated line asymmetry (Queloz et al. 2001; Mandushev et al. 2005). In the case of Kepler-10b, there is no evidence for a correlation between the bisector spans and the RVs which would otherwise argue against the planetary interpretation (see Figure 7), and similarly for the 45 day signal of KOI-72.02. However, we note that the uncertainties in the bisector span measurements are quite large so that the rms variation of the bisector spans (10.5 $\mathrm{m\,s^{-1}}$) exceeds the semi-amplitude of the RV variation ($3.3^{+0.8}_{-1.0}$ $\mathrm{m\,s^{-1}}$). Therefore, we do not consider the bisector span measurements to be discriminating in this case.

5. BLENDER ANALYSIS OF THE *KEPLER* LIGHT CURVE

In this section, we examine the possibility that the transit signals seen in the *Kepler* photometry of Kepler-10 are the result of contamination of the light of the target by an eclipsing binary along the same line of sight ("blend"). We consider as potential false positives physically associated hierarchical triple systems as well as chance alignments (eclipsing binary in the background or foreground). We make use of the technique referred to as BLENDER, described recently by Torres et al. (2010), which we apply separately to each of the signals in Kepler-10 since each could be due in principle to a separate blend. Briefly, this technique compares in a χ^2 sense the observed light curve to a synthetic light curve resulting from brightness variations of an eclipsing binary being attenuated by the (typically) brighter star Kepler-10. The parameters of the eclipsing binary are varied over wide ranges to find all viable blend scenarios producing a good match to the observations. The properties of each component of the binary (referred to here as the "secondary" and "tertiary") are taken from model isochrones (Marigo et al. 2008), and those of the main star (the "primary") are constrained by the spectroscopic analysis described earlier. For the technical details of BLENDER we refer the reader to the previously cited work, as well as Torres et al. (2004).

5.1. KOI-72.01 (Kepler-10b) Signal

Given the short period of this signal, we may assume that tidal forces have circularized the orbits of any potential eclipsing binary contaminants (Mazeh 2008). We considered first the case of a hierarchical triple system. Simulations with BLENDER clearly indicate that such systems in which the eclipsing binary is composed of two stars provide poor fits to the *Kepler* light curve. We thus rule out this type of blend scenario. If the eclipsing binary is composed of a planet (i.e., a smaller tertiary) transiting a star, rather than two stars eclipsing each other, then it is possible to reproduce the measured light curve, but only if the secondary has very nearly the same brightness as the target star itself. In that case, the resulting size of the tertiary is $\sqrt{2}$ larger than in a model of a single star transited by a planet. However, such a bright contaminant would have been evident in our spectroscopy as a second set of lines, and this case is therefore also excluded.

We next examined the background eclipsing binary scenario, allowing the relative distance between the binary and the main star to vary over a wide range. We accounted for absorption from dust along the line of sight as described by Torres et al. (2010), adopting a representative coefficient of differential extinction of $a_v = 0.5$ mag $\mathrm{kpc^{-1}}$. Interestingly, we found that no combination of relative distance and stellar properties for the eclipsing binary (composed in this case of two stars) gives an acceptable fit to the light curve. The reason is that

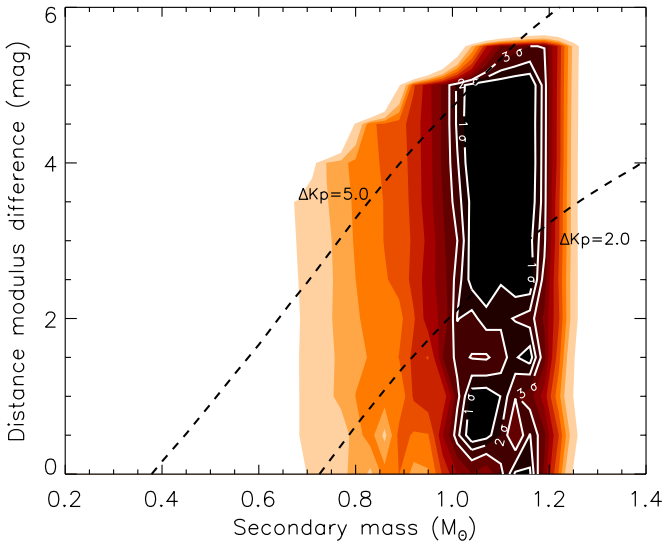

Figure 8. Map of the χ^2 surface corresponding to a grid of blend models for KOI-72.01 involving background eclipsing systems in which the tertiary is a (dark) planet, in a circular orbit around the secondary. Differential extinction is included (see the text). The vertical axis represents a measure of the relative distance between the background binary and the primary star, which we parameterize here for convenience in terms of the difference in distance modulus. Contours are labeled with the $\Delta\chi^2$ difference compared to the best planet model fit (expressed in units of the significance level of the difference, σ). Two dashed lines are also shown that correspond to equal magnitude difference (ΔKp) between the contaminating background binary and the primary star. Kinks in the contours are simply a result of the discreteness of the grid.

(A color version of this figure is available in the online journal.)

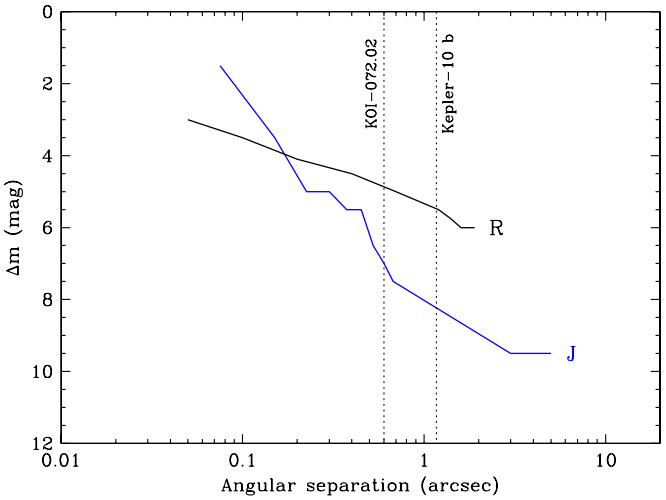

Figure 9. Sensitivity to faint companions near KOI-72 from our imaging observations. Any companions above the curves would be bright enough to be detected. *J*-band limits are from AO observations at the Palomar 200 inch telescope, and *R* is from speckle observations using the WIYN 3.5 m telescope. The vertical dotted lines indicate the 3σ confusion radius of 1.″17 for KOI-72.01 and 0.″60 for KOI-72.02, i.e., the maximum angular separation at which background eclipsing binaries would remain undetected in our centroid motion analysis.

(A color version of this figure is available in the online journal.)

all such blend configurations lead to out-of-eclipse brightness changes (ellipsoidal variations) with an amplitude so large as to be ruled out by the data. Thus, background blends of this kind can be confidently ruled out. This result is significant, because it reduces the overall likelihood of blends for KOI-72.01 considerably, as we describe below. If we allow the tertiary in the eclipsing pair to be a planet instead of a star (i.e., an object of smaller radius), then we do find a range of blend scenarios that lead to acceptable fits to the light curve, which cannot be ruled out a priori. This is illustrated in Figure 8, in which we show contours of equal goodness of fit of the light curve compared to a standard transit model fit. BLENDER indicates that these false positives can be up to about 5 mag fainter than the primary in the *Kepler* band, and that in all cases the secondary star is close in spectral type (and mass, or color) to the primary, or slightly earlier. Of these blends, we can further rule out those with secondaries having $\Delta Kp < 2$, which are bright enough that they would have been detected spectroscopically. This implicitly places a lower bound also on the size of the tertiaries ($\sim$3.8 $R_\oplus$), as tertiaries smaller than this limit only give good matches to the light curve if the contaminating star–planet pair is not too far behind the primary, and is therefore relatively bright.[28] Those cases would be ruled out spectroscopically, as mentioned before. The remaining blends shown in the figure above the line with $\Delta Kp = 2$ must be addressed statistically.

For this we followed closely the methodology applied by Torres et al. (2010) for the case of Kepler-9d. We computed the mean density of stars (i.e., background contaminants) in the appropriate mass range based on Figure 8 in half-magnitude bins, using the Besançon Galactic structure models of Robin et al. (2003), and we calculated the fraction of these stars that would remain undetected after our high-resolution imaging observations described earlier (the constraints from centroid motion analysis are less stringent; see Figure 9). Some of these stars might be orbited by (transiting) planets, constituting potential blends. To estimate how many of these cases one would expect, we adopted the same frequencies of transiting Jupiters and transiting Neptunes as in Torres et al. (2010), based on the results of Borucki et al. (2010b), adjusted in the case of the Neptune-size planets to account for the lower limit of $\sim$3.8 $R_\oplus$ allowed by BLENDER for the tertiaries. The outcome of these calculations is presented in Table 8. The total frequency of false positives (blend frequency, BF) we expect to find a priori for KOI-72.01 is BF $= 1.4 \times 10^{-8}$. Translating this into a probability statement for the planet likelihood is difficult, as argued by Torres et al. (2010), because it requires knowledge of the rate of occurrence of super-Earth-size planets, a quantity that is not yet in hand. Nevertheless, following those authors we may express the false-alarm rate for a random candidate star in the *Kepler* field generally as FAR $= N_{\rm FP}/(N_{\rm FP} + N_p)$, in which $N_{\rm FP}$ is the number of false positives and N_p is the unknown number of planets in the sample. The number of false positives may be taken to be $N_{\rm FP} = {\rm BF} \times 156{,}097 = 0.0022$, the product of the BF for KOI-72.01 and the total number of *Kepler* targets (Borucki et al. 2010b).

If we were to accept a confidence level of 3σ (99.73%) as sufficient for validation of a transiting planet candidate (corresponding to FAR $= 2.7 \times 10^{-3}$), then the minimum number of super-Earth-size planets required in order to be able to claim this level of confidence happens to be $N_p = 1$, according to the expression above. This value is so small that it gives us high confidence that the KOI-72.01 signal is not a false positive, but instead corresponds to a bona fide super-Earth-size planet. Another way to view this is that the expected number of background stars capable of producing the observed

[28] This lower limit of 3.8 $R_\oplus$ also excludes white dwarfs as possible tertiaries. Additionally, such massive objects in a tight 0.84 day orbit would lead to very significant ellipsoidal variation due to tidal distortions induced on the primary star, which are not seen.

Table 8
Blend Frequency Estimate for KOI-72.01 Based on the Frequencies of Transiting Giant Planets

Kp Range (mag)	Δ*Kp* (mag)	Stellar Density (deg^{-2})	ρ_{max} ($''$)	Stars ($\times 10^6$)	Transiting Jupiters 6–15 $R_\oplus$, $f_{Jup} = 0.11\%$ ($\times 10^{-6}$)	Transiting Neptunes 3.8–6 $R_\oplus$, $f_{Nep} = 0.074\%$ ($\times 10^{-6}$)
(1)	(2)	(3)	(4)	(5)	(6)	(7)
11.0–11.5	0.5	...	...	...	...	...
11.5–12.0	1.0	...	...	...	...	...
12.0–12.5	1.5	...	...	...	...	...
12.5–13.0	2.0	...	...	...	...	...
13.0–13.5	2.5	48	0.12	0.168	0.0002	0.0001
13.5–14.0	3.0	87	0.15	0.475	0.0005	0.0003
14.0–14.5	3.5	106	0.18	0.833	0.0009	0.0006
14.5–15.0	4.0	131	0.20	1.270	0.0014	0.0009
15.0–15.5	4.5	189	0.22	2.217	0.0024	0.0016
15.5–16.0	5.0	185	0.25	2.803	0.0031	0.0020
16.0–16.5	5.5	...	...	...	...	...
16.5–17.0	6.0	...	...	...	...	...
Totals		746	...	7.766	0.0085	0.0055

Blend frequency (BF) = $(0.0085 + 0.0055) \times 10^{-6} = 1.4 \times 10^{-8}$

Notes. Column 1: magnitude bins; Column 2: magnitude difference Δ*Kp* compared to the primary, taken at the upper edge of each bin; Column 3: density of stars from the Besançon models; Column 4: angular separation at which stars in the corresponding magnitude bin would go undetected in our imaging observations; Column 5: number of stars in a circle of radius ρ_{max} around KOI-72, restricted also by mass according to the contours in Figure 8; Column 6: number of expected transiting Jupiters as contaminants; Column 7: number of expected transiting Neptunes as contaminants.

signal is $\sim 8 \times 10^{-6}$ (see Table 8, bottom of Column 5), so the probability that what we are seeing is a background blend is $\sim 8 \times 10^{-6} \times P_{GP}/P_{SE}$, where P_{GP} and P_{SE} are the a priori probabilities that giant planets and super-Earths occur with short-period orbits. Thus, claiming a FAR corresponding to a 3σ detection only requires that the aforementioned probability ratio does not exceed 300.

It is worth noting that the arguments above allow us to validate KOI-72.01 independently of the detection of the reflex motion of the star (RVs). This is possible in this case because we are able to rule out, using BLENDER, all false positives in which the background eclipsing binary is composed of two stars, which are predicted to induce ellipsoidal variation at a level that is not present in the photometry. Were this not the case, the BF would have come out considerably larger, requiring in turn a significantly higher value for N_p.

5.2. The KOI-72.02 Signal

A similar BLENDER analysis was performed for KOI-72.02. For circular orbits, hierarchical triple systems are ruled out for the same reasons as in KOI-72.01. When considering the case of background eclipsing binaries (stellar tertiaries) with circular orbits, we find a range of blend scenarios that provide acceptable fits to the light curve, with secondaries of similar spectral type as the primary. Unlike the situation for KOI-72.01, the longer period of KOI-72.02 (45.3 days) leads to negligible ellipsoidal variation for the contaminating binaries, and this does not allow these types of blends to be excluded based on the quality of the fit, as we were able to do before. Chance alignment scenarios in which the tertiaries are planets rather than stars also lead to viable blends that can be up to 4 mag fainter than the target. Those that are brighter than $\Delta Kp = 2$ can be ruled out because they would have produced a spectroscopic signature, but fainter ones cannot be ruled out any other way if they are angularly close enough to the target to be unresolved by our imaging observations.

However, the longer period of this signal does not justify the assumption of a circular orbit. Allowing the orbit of a contaminating binary to have arbitrary eccentricity and also arbitrary orientation (longitude of periastron) can significantly increase the range of blends that provide good matches to the *Kepler* photometry, both for the chance alignment case and for physically associated triples. This is because the orbital speed in an eccentric orbit can be considerably larger or smaller than in a circular orbit, allowing for blends involving smaller or larger secondaries than would otherwise be permitted while still matching the observed duration of the transits, as described by Torres et al. (2010). It also increases the complexity of the problem, as the space of parameters to be explored is much larger. Additionally, because the secondaries are now not necessarily of the same spectral type as the primary star, attention must be paid to the resulting color of these blends, which could be different from the measured colors as reported in the KIC (Latham et al. 2005), in which case the blend would be excluded. Because these complications require significantly more effort to address, we are unable to provide sufficient evidence for the planetary nature of the KOI-72.02 signal at this time based on BLENDER considerations alone, and we defer such a study to a forthcoming publication. We note, however, that the transit duration and period of the two transit signals identified in the light curve give the same stellar density (1.142 ± 0.092 g cm^{-3} for KOI-72.01 versus 1.147 ± 0.096 g cm^{-3} for KOI-72.02) as derived from the transit properties using the analytic expression given in Equation (9) of Seager & Mallen-Ornelas (2003). This is a rare coincidence for a blend configuration.

6. STELLAR CHARACTERISTICS

6.1. Spectroscopic Parameters

We carried out an LTE spectroscopic analysis using the spectral synthesis package SME (Valenti & Piskunov 1996; Valenti & Fischer 2005) applied to a high-resolution

template spectrum from Keck–HIRES of Kepler-10 to derive an effective temperature, $T_{\rm eff} = 5705 \pm 150$ K, surface gravity, $\log g = 4.54 \pm 0.10$ (cgs), metallicity, [Fe/H] $= -0.15 \pm 0.03$, $v \sin i = 0.5 \pm 0.5$ km s^{-1}, and the associated error distribution for each of them. To refine the true parameters of the star, we took a novel path to constrain its surface gravity. The above effective temperature was used to constrain the fundamental stellar parameters derived via asteroseismic analysis (see Section 6.2). The asteroseismology analysis gave 4.341 ± 0.012 which is 0.2 dex lower than the SME value. The asteroseismology value is likely superior because of the high sensitivity of the acoustic periods to stellar radius. Still, the asteroseismology result depended on adopting the value of $T_{\rm eff}$ from SME. We recomputed the SME analysis by freezing (adopting) the seismology value for $\log g$. This iteration yielded values of $T_{\rm eff} = 5627 \pm 44$ K, [Fe/H] $= -0.15 \pm 0.04$, and rotational $v \sin i = 0.5 \pm 0.5$km s^{-1}. The revised effective temperature was then put back into the asteroseismology calculation to further constrain the stellar radius and gravity. This iterative process converged quickly, as the $\log g$ from seismology yielded an SME value for $T_{\rm eff}$ that was only slightly different from the original unconstrained determination.

We also measured the Ca II H&K emission (Isaacson & Fischer 2010), yielding a Mount Wilson S value, $S = 0.180$ and $\log R'_{\rm HK} = -4.89$. Thus Kepler-10 is a magnetically inactive star, consistent with its low rotational rate, $v \sin i = 0.5$ km s^{-1}. Thus, Kepler-10 appears to be an old (age greater than 5 Gyr) slowly rotating inactive star, slightly above the main sequence. This is consistent with the age derived from the asteroseismology analysis (Section 6.2).

6.2. Asteroseismology and the Fundamental Stellar Properties

With a magnitude in the *Kepler* bandpass of $Kp = 10.96$, Kepler-10 presented itself as a promising case for asteroseismic characterization and was, consequently, placed on the SC target list before it was even identified as a planet candidate. Figure 10(a) illustrates the power density spectrum of the SC light curve. It shows a clear enhancement of power, as expected for solar-like oscillations, around a frequency of 2500 μHz. In the spectrum one can identify sequences of approximately uniformly spaced peaks. This is in accordance with the asymptotic behavior of high-order acoustic modes, according to which the cyclic frequencies ν_{nl} approximately satisfy

$$\nu_{nl} \simeq \Delta\nu_0 (n + l/2 + \epsilon) - l(l+1) D_0 \qquad (1)$$

(Vandakurov 1967; Tassoul 1980), where n is the radial order and l is the spherical-harmonic degree of the mode. The large frequency separation $\nu_{nl} - \nu_{n-1\,l} \simeq \Delta\nu_0$ is essentially given by the inverse sound travel time across a stellar diameter; it is closely related to the mean stellar density $\rho_\star$, approximately satisfying $\Delta\nu_0 \propto \rho_\star^{1/2}$. For main-sequence stars D_0, giving rise to the small frequency separations $\nu_{nl} - \nu_{n-1\,l+2}$, is largely determined by the variation of sound speed in the core of the star and hence provides a measure of the evolutionary state of the star. Finally, ϵ is determined by conditions near the surface of the star.[29] (For details on the diagnostic potential of solar-like oscillations, see, for example, Christensen-Dalsgaard 2004). Photometric observations such as those carried out by *Kepler* are essentially restricted to degrees $l \leqslant 2$.

[29] Owing to the small value of $v \sin i$ we do not have to consider rotational effects on the frequencies.

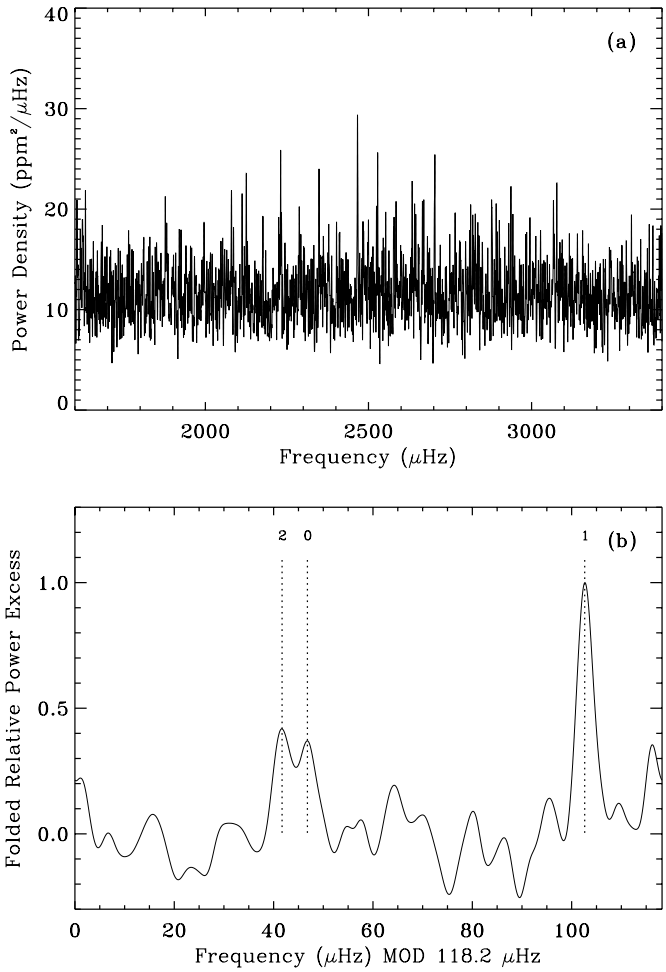

Figure 10. Panel (a) shows the power-density spectrum, with a 1.6 μHz smoothing, for short-cadence observations during the second month of Q2 and all of Q3. Panel (b) shows the spectrum folded at the large separation frequency of 118.2 μHz where the relative power excess is the power minus the noise floor, the result of which is divided by the peak power. This allows identification of the peaks corresponding to modes of degree $l = 0$, 1, and 2, as indicated.

The analysis of the observed frequency spectrum largely followed the procedures used by Christensen-Dalsgaard et al. (2010), with a pipeline developed for analysis of the *Kepler* p-mode data (Christensen-Dalsgaard et al. 2008; Huber et al. 2009). The first step was to carry out a correlation analysis to determine the large frequency separation $\Delta\nu_0$, leading to $\Delta\nu_0 = 118.2 \pm 0.2$ μHz. Using the scaling with the mean density and the corresponding values for the Sun, this yields a first estimate of $\rho_\star = 1.080 \pm 0.006$ g cm^{-3}. It should be noted, however, that this estimate does not take into account detailed differences between the structure of the star and the Sun.

The next step in the analysis was to identify individual modes in the frequency spectrum. The detailed structure of the spectrum is illustrated in Figure 10(b) which shows the folded spectrum, i.e., the sum of the power as a function of the frequency modulo $\Delta\nu_0$. As indicated, in accordance with Equation (1) there is clearly a pair of closely spaced peaks, corresponding to $l = 2$ and 0, as well as a single peak for $l = 1$. Given this identification, we were able to determine the individual frequencies of 19 modes. These are illustrated in an échelle diagram (cf. Grec et al. 1983, see below) in Figure 11.

To determine the stellar properties, we fitted the observed frequencies to a grid of models. These were computed using

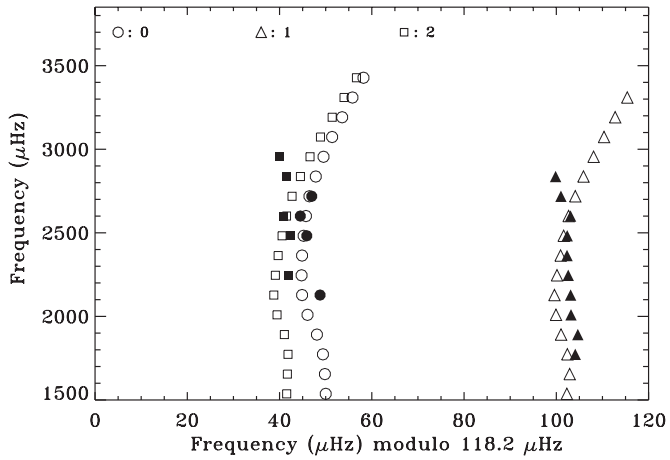

Figure 11. Échelle diagram (cf. Grec et al. 1983) illustrating the observed frequencies (filled symbols) and the frequencies of one of the best-fitting model (open symbols), for modes of degree $l = 0$ (circles), $l = 1$ (triangles), and $l = 2$ (squares). The model has a mass of 0.9 $M_\odot$, $Z = 0.0144$, $\alpha_{\rm ML} = 1.8$, and an age of 11.6 Gyr.

the Aarhus Stellar evolution and pulsation codes (Christensen-Dalsgaard 2008a, 2008b). See also Christensen-Dalsgaard et al. (2010). Diffusion and settling of helium and heavy elements were neglected. The grid consisted of models of mass between 0.8 and 1.1 $M_\odot$ in steps of 0.02 $M_\odot$ and mixing length $\alpha_{\rm ML} = 1.5$, 1.8, and 2.1. The composition was characterized by heavy-element abundances $Z = 0.011, 0.0127$, and 0.0144, corresponding to the observed [Fe/H] $= -0.15 \pm 0.06$ (see above); this assumes a solar surface ratio between the heavy-element and hydrogen abundances $(Z_{\rm s}/X_{\rm s})_\odot = 0.0245$ (Grevesse & Noels 1993), and with the initial hydrogen abundance X_0 related to Z, from galactic chemical evolution, through $X_0 = 0.7679 - 3Z_0$.

For each model in the grid we calculated an evolution track extending well beyond the end of central hydrogen burning and, for the relevant models along the track, we computed adiabatic frequencies for modes of degree $l = 0$–2. The match between the observed and computed frequencies, $\nu_{nl}^{\rm (obs)}$ and $\nu_{nl}^{\rm (mod)}$, was characterized by

$$\chi^2_\nu = \frac{1}{N-1} \sum_{nl} \left(\frac{\nu_{nl}^{\rm (obs)} - \nu_{nl}^{\rm (mod)}}{\sigma_\nu} \right)^2 , \quad (2)$$

where N is the number of observed frequencies and σ_ν is the standard error in the observed frequencies, which we estimated as 1 μHz. In the fit we also considered the observed effective temperature $T_{\rm eff}$ (see above), using as combined measure of the goodness of fit

$$\chi^2 = \chi^2_\nu + \left(\frac{T_{\rm eff}^{\rm (obs)} - T_{\rm eff}^{\rm (mod)}}{\sigma(T_{\rm eff})} \right)^2 , \quad (3)$$

where $T_{\rm eff}^{\rm (obs)}$ and $T_{\rm eff}^{\rm (mod)}$ are the observed and model values and $\sigma(T_{\rm eff})$ is the standard error in $T_{\rm eff}$.

Along each evolution track we determined that model which minimized χ^2, among the discrete timesteps in the evolution sequence. The final best model corresponding to the track was obtained by further minimizing χ^2 to determine $\chi^2_{\rm min}$ for that track, interpolating $T_{\rm eff}$ linearly between timesteps and scaling the frequencies according to $\rho_\star^{1/2}$. Given the resulting model values for all evolution tracks, we determined the final estimates of the stellar properties as an average over all tracks, weighted by $\chi^{-2}_{\rm min}$.

A preliminary application of this procedure, using the value $T_{\rm eff} = 5705 \pm 150$ K as described in the preceding section, resulted in an average surface gravity of $\log g = 4.341 \pm 0.012$, substantially different from the spectroscopically determined value of 4.54 ± 0.10. In view of the known problems with the spectroscopic determination of $\log g$ we repeated the spectroscopic analysis, fixing $\log g$ as 4.341 ± 0.012 in accordance with the asteroseismic inference. This resulted in $T_{\rm eff} = 5627 \pm 44$ K. We then repeated the asteroseismic fits, conservatively increasing the uncertainty in $T_{\rm eff}$ to 60 K. This resulted in the final estimates of the stellar parameters presented in Table 7: $M_\star = 0.895 \pm 0.060\, M_\odot$, $R_\star = 1.056 \pm 0.021\ R_\odot$, $\rho_\star = 1.068 \pm 0.008$ g cm^{-3}, and age $= 11.9 \pm 4.5$ Gyr. The distance of 173 ± 27 pc is computed using the g-band SDSS apparent magnitude in the KIC and bolometric corrections interpolated form the tables of Girardi et al. (2008).

To illustrate the quality of the fit, Figure 11 shows the observed frequencies and the frequencies for the best-fitting model in an échelle diagram, reflecting the asymptotic structure of the spectrum described by Equation (1). In accordance with this equation, the spectrum has been divided into segments of length $\Delta\nu_0$ which have been stacked. Formally this corresponds to reducing the frequencies modulo $\Delta\nu_0$. The asymptotic behavior is reflected in the nearly vertical columns of points, corresponding to the different values of the degree. Also, it is clear that the model provides a reasonable, although far from perfect, fit to the observations.[30]

7. PLANET CHARACTERISTICS

The physical and orbital properties of both transit signatures are derived by simultaneously fitting *Kepler* photometry and Keck RVs and by adopting the mean-stellar density of the host star as determined by asteroseismology. Our system model uses the analytic formalization of Mandel & Agol (2002) to fit photometric observations of the transit. We use the fourth-order nonlinear parameterization of limb darkening also described by Mandel & Agol (2002) with coefficients ($c_1 = 1.086$, $c_2 = -1.366$, $c_3 = 1.823$, $c_4 = -0.672$) calculated by Prsa (2010) for the *Kepler* bandpass. We account for variability phased to the orbital period by including the effects of reflected and emitted light from the planet, ellipsoidal variations due to tidal distortions of the host star and Doppler boosting due to motion of the star around the center of mass. For reflected/emitted light, we assume that the phased light curve is reproduced by a Lambertian reflector scaled by the geometric albedo. Ellipsoidal variations are modeled by using the prescription of Pfahl et al. (2008). Doppler boosting uses the methodology outlined in van Kerkwijk et al. (2010). We model the occultation by computing the fraction of the planet occulted by the star as a function of the star–planet projected distance. We assume that the planet is a uniformly illuminated disk during occultation.

Our model parameters are the stellar mass and radius ($M_\star$, $R_\star$), the planet mass and radius ($M_{\rm P}$, $R_{\rm P}$), the orbital inclination (i), eccentricity ($e \cos w$, $e \sin w$), the geometric albedo (A_g), and the RV amplitude and zero point (K, V_0). Model fits to the Kepler-10b light curve yield an eccentricity that is consistent with zero ($e \cos w = 0.02 \pm 0.10$; $e \sin w = -0.13 \pm 0.20$)

[30] It may be noted that, unlike the simple expression (1), the small separation between modes with $l = 0$ and 2 depends on frequency.

which is consistent with our expectations for tidal circularization (Mazeh 2008). Given the large orbital separation of the outer planet candidate, we can not assume its orbit to be circular based on tidal circularization. The small predicted RV amplitude prevents a measurement of the eccentricity from existing RV observations. The duration of the transit for the outer planet candidate is consistent with a circular orbit, but the resulting upper limit is still significant ($e \simeq 0.2$). For the remainder of our discussion, the models are constrained to zero eccentricity for both Kepler-10b and KOI-72.02. The RV variations are modeled by assuming non-interacting (Keplerian) orbits. If KOI-72.02 were to be confirmed, then the relative inclination between the two orbits is likely less than 20°, as larger relative inclinations would require a fortuitous alignment of the orbital nodes for both planets to transit (Ragozzine & Holman 2010).

We initially fit our observations by fixing $M_\star$ and $R_\star$ to their asteroseismic values (see Section 6.2). Model parameters are found by chi-squared minimization using a Levenberg–Marquardt prescription. We then use the best-fit values to seed a Markov Chain Monte Carlo (MCMC) parameter search (Ford 2005) to fit all model parameters. We adopt the uncertainty on the asteroseismic determined mean-stellar density as a prior of the stellar mass and radius. A Gibbs sampler is used with widths initially defined by uncertainties derived from the diagonals of the constructed co-variance matrix (Ford 2006). Our Markov chain contains 194,066 elements. We list the median of the distribution for each model parameter in Table 7 and the corresponding ±68.3% credible intervals (akin to a 1σ confidence interval) centered on the median. The resulting properties of Kepler-10b are as follows: $M_{\rm P} = 4.56^{+1.17}_{-1.29}\ M_\oplus$, $R_{\rm P}$=$1.416^{+0.033}_{-0.036} R_\oplus$, $\rho_{\rm P} = 8.8^{+2.1}_{-2.9}$ g cm^{-3}, and a surface gravity ($3.35^{+0.11}_{-0.13}$ dex) that is just 2.3 times that of Earth. Our knowledge of the planet is only as good as our knowledge of the parent star. Here, the planet radius is determined with a precision of just over 2%—comparable to the precision of the stellar radius derived from asteroseismology. The precision of the planet mass, however, is driven by the low semi-amplitude of the RVs ($3.3^{+0.8}_{-1.0}$ m s^{-1}) relative to the internal errors (1.5–2 m s^{-1}).

The absence of a statistically significant orbital signature in the RV data at the 45 day period of KOI-72.02 translates to an upper limit for the mass under the planet interpretation. The best fit to the RVs, constrained by the photometric period and phase, yields a slightly negative semi-amplitude and, consequently, a mathematically valid but physically unrealistic negative planet mass: $M_{\rm P} = -2.80^{+6.33}_{-6.52}\ M_\oplus$. Of more relevance is the distribution of the masses returned by the MCMC calculations. The upper mass limit is taken to be three times the 68.3% credible interval (6.5 $M_\oplus$) or 20 $M_\oplus$. This is the upper limit reported in Table 7.

The phase-folded light curves together with the model fit are shown in the lower two panels of Figure 12. The best fit for Kepler-10b requires a phase modulation with an amplitude of 7.6 ± 2.0 ppm and a 5.8 ± 2.5 ppm occultation, both of which are shown in the scaled and phase-shifted light curve in Figure 13. The modeled RV variations for Kepler-10b are shown in Figure 6 as a function of orbital phase together with the 40 Doppler measurements (small circles) and the same averaged over 0.1 phase bins (large circles).

The parameters derived from the MCMC analysis are listed in Table 7 and discussed in Section 9. Parameters such as planet mass, radius, and density for KOI-72.02 are included in the table for completeness. However, the reader is cautioned against overinterpretation since the KOI-72.02 transits have not yet been confirmed to arise from a planetary companion.

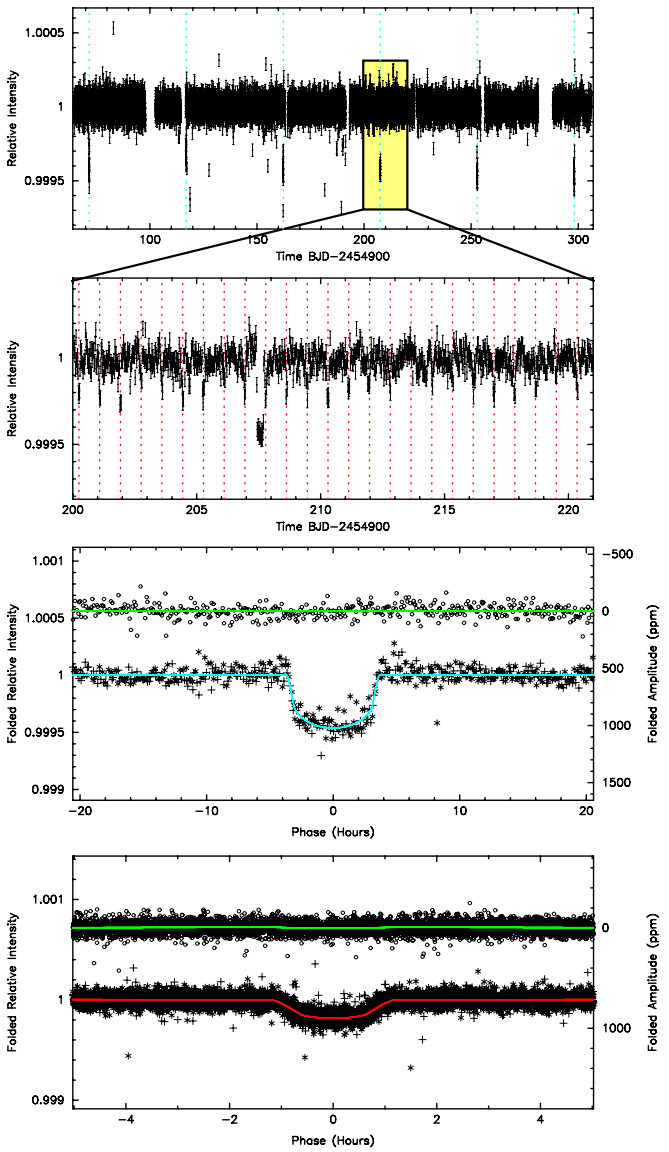

Figure 12. *Kepler* photometry and physical models are plotted as a function of both time (upper two panels) and phase (lower two panels). The transits of KOI-72.02 are highlighted by blue vertical lines in the topmost panel while a cutout (defined by the yellow box) is expanded to show the transits of Kepler-10b highlighted by red vertical lines (second from top). The bottom two panels show the phase-folded light curves centered on phase zero as defined by the central transit time. The modeled light curves are shown as colored lines (blue corresponding to KOI-72.02 and red corresponding to Kepler-10b. Also shown is a phase cutout of the light curve and model (green) centered on phase = 0.5 where occulations would occur for a circular orbit. The relative intensity scale for phase = 0 can be read off the *y*-axis on the left-hand side of the plot while the relative intensity scale for phase = 0.5 can be read off the *y*-axis on the right-hand side of the plot.

8. STATEMENTS ABOUT TRANSIT TIMING VARIATIONS

To measure the transit times, we generate a template transit shape based on folding the light curve with the given linear ephemeris. For each transit, we estimate the transit time by performing a local minimization, varying the transit mid-time, the light curve normalization, and the light curve slope (outside

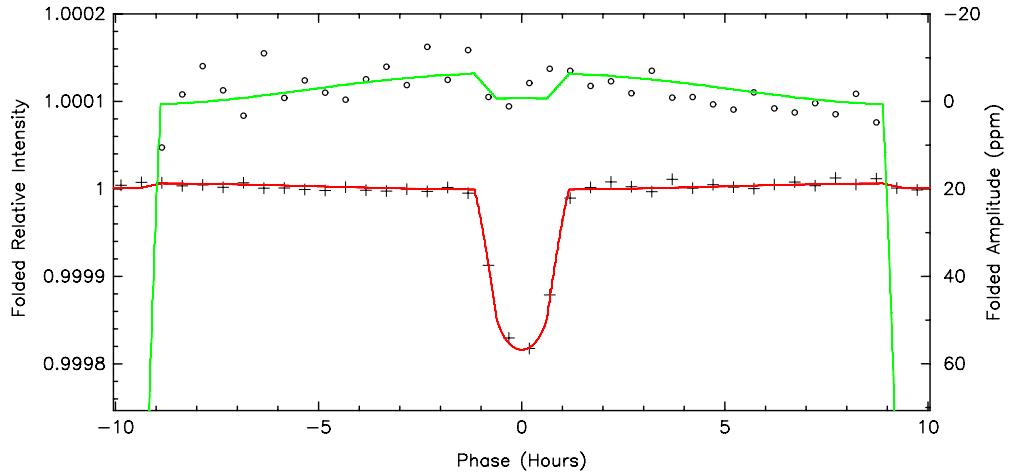

Figure 13. Relative intensity scale of the phase-folded light curve of Kepler-10b shown in the bottom panel of Figure 12 is expanded to show the phase modulation and marginal occultation required by the model fits. Colors have the same meaning as in Figure 12.

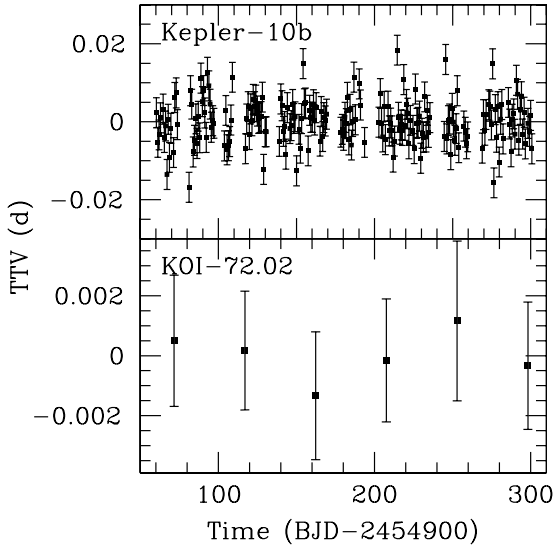

Figure 14. Difference between each best-fit transit time and a linear ephemeris for Kepler-10b (top) and KOI-72.02 (bottom). As expected, we do not detect any statistically significant transit timing variations.

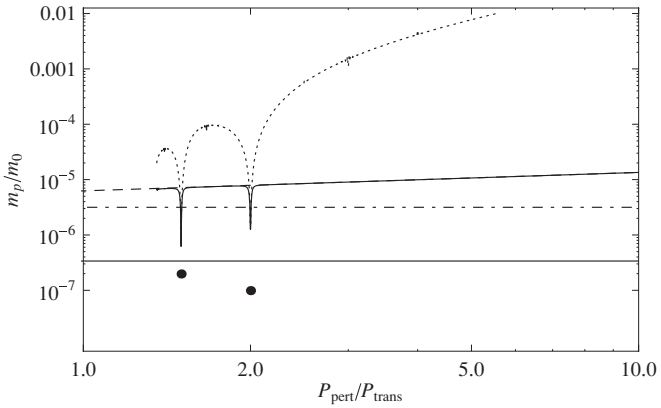

Figure 15. Constraints (95% confidence level) on low-eccentricity secondary planets that are exterior to Kepler-10b as a function of the period ratio using the measured transit times and RV data. The dotted curve shows the limit from a TTV analysis alone from Equation (A7) in Agol et al. (2005). The dashed line is the expected sensitivity from 40 RV measurements with 2.6 m s^{-1} precision calculated using Equation (2) from Steffen & Agol (2005). The solid curve is the overall sensitivity from both RV and TTV measurements (summed in quadrature). The diamonds are calculations for MMR from Equation (33) in Agol et al. (2005). The TTV sensitivity curve has been scaled down by $\sqrt{269}$ to represent the improvement in sensitivity due to the number of observed transits. Finally, the horizontal dot-dashed and triple-dot-dashed lines correspond to the mass of the Earth and the mass of Mars, respectively.

of transit), but holding the remaining parameters (planet–star radius ratio, transit duration, impact parameter, and limb darkening) fixed. We iterate to improve the template transit shape used for measuring the transit times. The results are shown in Figure 14. The true uncertainties may be larger than the formal uncertainties (indicated by error bars), particularly for Kepler-10b. Regardless, we do not detect statistically significant TTVs for Kepler-10b at levels above 0.01 days and for KOI-72.02 at levels above 0.003 days. Given the masses and periods we measured for both planet candidates, we predicted that TTVs would not be detectable, as indeed is the case.

The precision with which the transit times of Kepler-10b can be measured is lessened by the small size of the planet. Coupled with this loss in timing resolution, the period of the planet is also quite short at less than a day. Thus, the ratio of the period to the timing precision (the S/N) is only $P/\sigma \simeq (75{,}000\,\mathrm{s})/(500\,\mathrm{s}) = 150$. For comparison, a Jupiter-size planet (∼1% transit depth) in a 1 week orbit would produce a ratio about 100 times larger. The TTVs from a nonresonant perturbing planet are essentially independent of the mass of the transiting planet. To summarize, additional non-transiting planets orbiting Kepler-10 are not well constrained by the measured transit times of Kepler-10b. Here, our RV measurements, which have very good precision of approximately 2.6 m s^{-1}, are better suited to detect additional, nontransiting planets in this system.

The small mass of this planet does provide good sensitivity to resonant perturbing planets where the TTV signal scales with the ratio of planet masses (see Equation (33) of Agol et al. 2005). Figure 15 shows the maximum allowed mass of a perturbing planet in an orbit near Kepler-10b including both the transit time and RV data. Near mean-motion resonance, small planets with masses below that of Mars can be excluded. Away from resonance, the RV data constrain the presence of additional planets to be less than a few Earth masses.

If KOI-72.02 is, indeed, a longer-period planet orbiting Kepler-10, a TTV signal due to the interaction with Kepler-10b must exist at some level and it behooves us to consider the

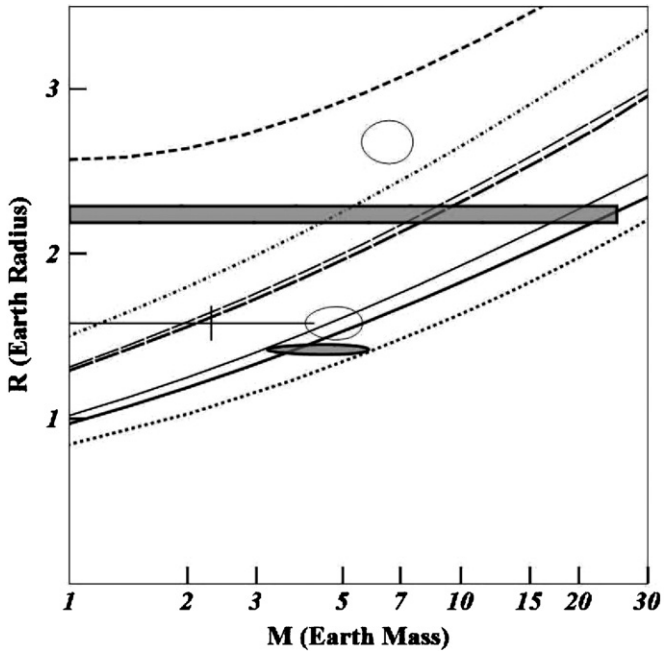

Figure 16. Kepler-10b and KOI-72.02 on the mass–radius diagram. Kepler-10b is shown with a 1σ ellipse at $R_p = 1.416 R_E$; KOI-72.02 is shown with a 1σ band, constrained in mass below $\approx 25 M_E$. Two similar planets are shown for comparison: GJ1214b (1σ ellipse top) and CoRoT-7b (1σ ellipse below, and solid crossed lines for the alternative mass estimate as described in the text). Theoretical models are shown as curves (from top to bottom): 10% by mass H/He envelope with typical ice giant interior similar to Uranus and Neptune (short-dashed line); theoretical pure water object (dot-dashed line); 50% water planets with 34% silicate mantle and 16% Fe core (thick long-dashed line), or with a low Fe/Si ratio of 44% mantle and 6% Fe core (thin long-dashed line); and Earth-like composition with the same Fe/Si ratios (thick and thin solid lines). Models are from the grid of Zeng & Sasselov (2011). The dotted curve at the bottom corresponds to a maximum Fe core fraction expected from simulations of mantle stripping by giant impacts (Marcus et al. 2010).

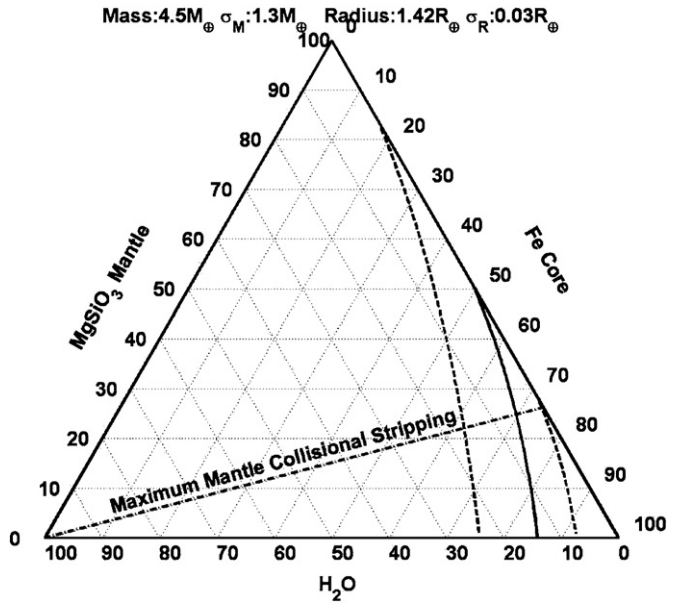

Figure 17. Interior structure models for Kepler-10b shown on a ternary diagram, illustrating the planet's solid nature. Three possible bulk materials can mix to determine a planet's radius at a fixed planet mass. The model planet radius appears as a curved line; this iso-radius curve for Kepler-10b (solid line) lies very close to the "dry side" of the ternary diagram, indicating that most models at this high density exclude water as a significant bulk component of the planet's composition. The dash-dotted line corresponds to a maximum Fe core fraction expected from simulations of mantle stripping by giant impacts (Marcus et al. 2010).

expected magnitude of such a signal and whether or not it would be detectable in the data at hand. The hierarchical architecture limits the mechanisms that are capable of inducing a detectable signal. Neither changes in the light travel time caused by the displacement of the star due to a hypothetical outer planet, nor an evolving tidal field caused by an eccentric outer planet (see Section 4 of Agol et al. 2005), would be detectable in this system given the measured timing uncertainties. This statement is true even when one accounts for the factor of $\sqrt{N_{\rm trans}}$ (where $N_{\rm trans}$ is the number of observed transits) statistical improvement in the sensitivity. A scenario with an outer planet having a large eccentricity would only produce a detectable signal if its mass is comparable to Jupiter and its eccentricity is greater than 0.95 (see Equation (25) of Agol et al. 2005). Consequently, the absence of a TTV signal in the data does not rule out the planetary interpretation of KOI-72.02, given the upper mass limit of 20 $M_\oplus$ (Section 7).

9. DISCUSSION

9.1. Composition of Kepler-10b

Kepler-10b is a high-density rocky planet. This conclusion is based on the comparison of its radius and mass, measured within 1σ, with theoretical calculations of interior structure, as illustrated in Figures 16 and 17. The conclusion accounts for known uncertainties in the theory.

Figure 16 is the mass–radius diagram for small planets in units of Earth mass and radius (after Zeng & Sasselov 2011). Earth lies on the left edge, between two models (solid lines) of Earth-like composition with a range of Fe/Si ratios. Uranus and Neptune are out of range, above the upper right portion of the diagram. Kepler-10b (bottom 1σ ellipse) and KOI-72.02 (1σ band with upper limit in mass at $\approx 25 M_E$) are shown with models and with two other planets known in this size range: CoRoT-7b and GJ1214b. In Figure 16, the upper 1σ ellipses are for GJ 1214b (Charbonneau et al. 2009) and CoRoT-7b (Queloz et al. 2009 for mass; Bruntt et al. 2010 for radius). The uncertainty in the mass of CoRoT-7b is dependent on the methodology used to correct for the stellar activity signal that dominates the Doppler data. For example, Queloz et al. (2009) compute a mass of $4.8 \pm 0.8\, M_\oplus$, while Ferraz-Mello et al. (2010) obtain $8.5 \pm 1.5\, M_\oplus$. Hatzes et al. (2010) compute a mass of $6.9 \pm 1.5\, M_\oplus$, while Pont et al. (2010) obtain $2.3 \pm 1.8\, M_\oplus$. The mass of CoRoT-7b, provided by Pont et al. (2010), is shown by straight solid lines in Figure 16 in order to illustrate the range of mass values present in the literature.

Theoretical calculations in Figure 16 are shown as curves, which are (from top to bottom): 10% by mass H/He envelope with typical ice giant interior similar to Uranus and Neptune (short-dashed line); theoretical pure water object (dot-dashed line); 50% water planets with 34% silicate mantle and 16% Fe core (thick long-dashed line), or with a low Fe/Si ratio of 44% mantle and 6% Fe core (thin long-dashed line; and Earth-like composition with the same Fe/Si ratios (thick and thin solid lines). These models are from the grid by Zeng & Sasselov (2011), based on Valencia et al. (2007) with many updates, e.g., new water EOS by French et al. (2009). The Fe/Si ratios chosen in this grid correspond to the range observed in the solar system given a stellar Fe/Si range in the solar neighborhood (Grasset

et al. 2009), where the low Fe/Si ratio corresponds to the lowest values measured in small bodies in the outer solar system, namely Ganymede. Note that the hypothetical 100% water and H/He envelope model curves are shown for illustration only; given the extremely high equilibrium temperature of Kepler-10b an extended hot atmosphere of such volatiles has to be accounted for separately, but Kepler-10b is too dense for these scenarios.

The interior structure of GJ 1214b has been modeled as an $H/He/H_2O$ planet with a rocky core (Nettelmann et al. 2010). Indeed, it lies between the models of ice giants similar to Neptune and Uranus and the models of a 50% water planet. And while the Queloz et al. (2009) mass and radius point to a rocky composition, the lower mass of Pont et al. (2010) marginally favors a water/ice composition. The properties of Kepler-10b together with their uncertainties clearly indicate a high-density, rocky planet.

The dotted curve at the bottom of Figure 16 is the envelope corresponding to a maximum Fe core fraction expected from simulations of mantle stripping by giant impacts (Marcus et al. 2010). These simulations and planet formation scenarios indicate that pure Fe core objects cannot form in the mass range we consider. At the mass of Kepler-10b these simulations predict that the maximum attainable Fe core is about 75% by mass. For comparison, Mercury has a ≈70% Fe core.

Theoretical calculations of the interiors of high-density planets suffer from a number of uncertainties in equations of states, high-pressure phases of materials inaccessible to lab experiments, cooling and differentiation histories, etc. There is consensus in the literature (Valencia et al. 2006, 2007; Fortney et al. 2007; Seager et al. 2007; Grasset et al. 2009) regarding the general results. However, the theoretical uncertainties are compounded by a degeneracy between only two observables (radius and mass), and three or four distinct types of bulk materials: Fe core, mantle (silicates, etc.), water, and hydrogen/helium gas (see Valencia et al. 2007; Rogers & Seager 2010 for details).

At very high densities, the radius of solid planets is constrained by the lack of bulk materials with density and compression properties above that of Fe and Fe alloys (see lower-envelope dotted curve in Figure 16). Planets with high densities close to that envelope are likely composed predominantly of silicates and Fe; the degeneracy is lifted as indicated by the curvature of the iso-radius curves when they approach asymptotically the "dry" right-hand side of the ternary diagram in Figure 17.

Ternary diagrams were introduced to studies of solid planet structure by Valencia et al. (2007). The three axes of the ternary diagram represent the core, mantle, and ice fraction of a planet of a given mass (in this case, the mass derived for Kepler-10b). The axes are read by following lines parallel to the edges so that the three mass fractions sum to unity. Although there are six radiants emerging from each point in the grid, only three will result in mass fractions that add to unity. Different combinations of core, mantle, and ice fraction yield a planet radius that can be computed with theoretical models constrained by a given mass. Radius is not unique to a specific combination of mass fractions. The solid line in Figure 17 is an iso-radius. It shows the possible combinations that all yield the derived radius of Kepler-10b. The dotted lines provide bounds on the domain captured by the 1σ errors in planet radius. A ternary diagram represents a cross-section at a given mass. However, mass-dependent uncertainties are included in the error bars represented by the dotted line. The iso-radius together with the 1σ error bars are a good representation of the possible bulk compositions for a given planet.

The degeneracy in bulk composition discussed above is best illustrated in Figure 17, as a planet defined by a mass and radius is represented by a curve (solid) that can span a range of iron:mantle:water fractions. This degeneracy is practically lifted only for very high density planets near the "dry" right-hand side, close to the 100% iron core vertex, because (1) the iso-radius curves bend as they approach the 0% water level, and (2) the H_2O and OH molecules are able to be incorporated inside high-pressure silicate phases without changing their EOS much. For Kepler-10b, the combination of very high density and constraints from mantle-stripping simulations (dash-dotted line), restrict its bulk compositions to dry rocky iron-core-dominated interiors similar to Mercury. On the other hand, if the observational derivation of the mass of Kepler-10b were significantly overestimated (by more than 1σ), the planet could contain significant amount of water in its interior.

In conclusion, within 1σ–2σ in its derived radius and mass, the planet Kepler-10b is a dry rocky planet with high Fe content. Its high density does not violate the prediction for maximum mantle stripping during planet formation (Marcus et al. 2010).

9.2. The Phase Curve of Kepler-10b

The phase curve amplitude of Kepler-10b is 7.6 ± 2.0 ppm. If due to scattered light alone, this corresponds to a *Kepler* bandpass effective geometric albedo of 0.68. The occultation depth is 5.8 ± 2.5 ppm which corresponds to an effective geometric albedo of 0.61 ± 0.17. This is an unusually high albedo. The only known solar system bodies that are so bright are Venus (due to photochemically induced hazes) and Saturn's icy moon Enceladus (coated with fresh ice). Kepler-10b is likely too hot for any hazes and is certainly too hot for any ice. Another possibility is that Kepler-10b has silicate clouds, but they would have to be completely covering the planet's day side and have a large particle size in order to provide the required reflectivity (see, for example, Seager et al. 2000).

We prefer an interpretation that the phase curve is dominated by a thermal radiation change from the planet's day to night side. This case would be reminiscent of hot Jupiters, which have a hotter day side than night side. In the case of the *Kepler* bandpass, the temperature difference need not be too extreme, as long as the planet is hot enough on the day side (as is the case for Kepler-10b with a equilibrium temperature of 1833 K). This is because the *Kepler* bandpass is in the optical, and so the contribution of thermal radiation drops off rapidly with decreasing temperature (i.e., day-to-night side). In other words, a passband on the Wien side of the black body curve will capture significantly different fluxes with just a small change in temperature. An example of this is the phase curve of HAT-P-7 (Borucki et al. 2009; Welsh et al. 2010).

An intriguing possibility is that Kepler-10b has no atmosphere at all, having lost it over time due to atmospheric erosion. One test is to search for a hotspot directly at the substellar point, since no atmospheric winds would be available to move the hotspot off center (Seager & Deming 2009). Further *Kepler* data, in particular a confirmation and robust measurement of the occultation depth, of Kepler-10b will help with any interpretation.

Asteroseismic measurements of the host star Kepler-10 indicate that the planetary system is very old, allowing for more

than 11 Gyr of evaporation and mass loss from the surface of Kepler-10b. Assuming, as is common, that the planet arrived at its present orbit within about 100 Myr of formation, the relevant evaporation time scales are those of water steam or a silicate surface. Any H/He envelope would have evaporated too quickly (at $\approx 10^{11}$ g s^{-1}) to affect the further evolution of the planet, while the evaporation of the silicate mantle is too slow to remove more than 50% of the planet's original mass (Valencia et al. 2009). Therefore, it is difficult to establish if Kepler-10b is the remnant core of a water planet or an ice giant planet, though it is probable that it must have lost a significant fraction of its mass.

10. SUMMARY

NASA's *Kepler* Mission collects transit photometry from a spaceborne Schmidt camera to detect and characterize extrasolar planets with the goal of determining the frequency of Earth-size planets in or near the habitable zone of Sun-like stars. Now in its second year of operation, the mission has reached an important milestone toward meeting that goal, namely the discovery, reported herein, of its first rocky planet, Kepler-10b. This planet was identified via transit photometry. The analyses described here are based on ~8 months of *Kepler* 29.4 minute cadence data acquired between 2009 May 2 and 2010 January 9. The target was also observed at a higher 1 minute cadence from 2009 July 21 to 2009 August 19 and 2009 September 18 and 2010 January 9.

Two distinct sets of transit events were detected in the light curve of Kepler-10 constructed from ~8 months of *Kepler* photometry: (1) a 152 ± 4 ppm dimming lasting 1.811 ± 0.024 hr with transit ephemeris of $T[\mathrm{BJD}] = 2454964.57375^{+0.00060}_{-0.00082} + N * 0.837495^{+0.000004}_{-0.000005}$ days and (2) a longer-period event described by a 376 ± 9 ppm dimming lasting 6.86 ± 0.07 hr and an ephemeris $T[\mathrm{BJD}] = 2454971.6761^{+0.0020}_{-0.0023} + N * 45.29485^{+0.00065}_{-0.00076}$ days. Statistical tests on the photometric and individual pixel flux time series of Kepler-10 established the viability of the planet candidates. For example, comparison of the flux-weighted photocenter during transit and outside of transit revealed no deviation consistent with an eclipse event associated with one of the nearby stars that might be diluting the light curve of Kepler-10. Clean statistics triggered a battery of ground-based follow-up observations.

High-resolution reconnaissance spectroscopy was used to verify the effective temperature and surface gravity as well as rule out obvious eclipsing binaries masquerading as planets by way of moderate-precision RVs. High spatial resolution imaging (AO and Speckle) was acquired to identify faint, nearby stars that should be considered in the photocenter analysis as potential background eclipsing binaries. In the case of Kepler-10, no additional stars were identified. Forty precision Doppler measurements were acquired with the Keck 10 m telescope between 2009 May and August. These measurements confirmed the planetary nature of the short-period transit event. The photometric period was clearly seen in a periodigram of the velocities, and the variations are phased as expected given the transit epochs. With a semi-amplitude of just $3.3^{+0.8}_{-1.0}$ m s^{-1}, the Doppler measurements suggest a planetary mass for this companion. No significant signal was detected in the measurements at the photometric period of the outer candidate, KOI-72.02.

Knowledge of the planet is only as good as our knowledge of the star it orbits. Matching the reconnaissance spectroscopy of Kepler-10 to a library of synthetic spectra yielded $T_{\mathrm{eff}} = 5680 \pm 91$ K, $\log g = 4.33 \pm 0.16$, $[\mathrm{Fe/H}] = -0.09 \pm 0.04$, and $v \sin i = 1.5 \pm 0.5$ km s^{-1}. Full spectral synthesis using HIRES echelle data without the iodine cell yielded $T_{\mathrm{eff}} = 5705 \pm 150$ K, $\log g = 4.54 \pm 0.10$, $[\mathrm{Fe/H}] = -0.15 \pm 0.03$, and $v \sin i = 0.5 \pm 0.5$ km s^{-1}. Because the parent star is relatively bright ($Kp = 10.96$) and, hence, amenable to asteroseismic analysis, *Kepler* photometry was also collected at 1 minute cadence for ~5 months from which we detected 19 distinct pulsation frequencies. Modeling of these frequencies resulted in precise knowledge of the fundamental stellar parameters. The process was iterated once in that the asteroseismic analysis yielded a surface gravity of $\log g = 4.341 \pm 0.012$ which was then fixed in the spectral synthesis analysis to yield an improved effective temperature, $T_{\mathrm{eff}} = 5627 \pm 44$ K, that was then fed back to the asteroseismic analysis. The result is that Kepler-10 is a relatively old (11.9 ± 4.5 Gyr) but otherwise Sun-like main-sequence star with $T_{\mathrm{eff}} = 5627 \pm 44$ K, $M_\star = 0.895 \pm 0.060\ M_\odot$, and $R_\star = 1.056 \pm 0.021\ R_\odot$.

Physical models, constrained by the asteroseismology-derived stellar parameters, were simultaneously fit to the transit light curves and the precision Doppler measurements. Modeling produced tight constraints on the properties of Kepler-10b: $M_{\mathrm{P}} = 4.56^{+1.17}_{-1.29}\ M_\oplus$, $R_{\mathrm{P}} = 1.416^{+0.033}_{-0.036} R_\oplus$, and $\rho_{\mathrm{P}} = 8.8^{+2.1}_{-2.9}$ g cm^{-3}. Evaluation of these properties within a theoretical framework allowed us to draw conclusions about the planet's composition. Within 1σ–2σ of the derived mass and radius, Kepler-10b is a dry, rocky planet with high Fe content. Its high density does not violate predictions for maximum mantle stripping during planet formation.

The authors thank Carly Chubak for computing the barycentric radial velocity of Kepler-10. J.C.D. acknowledges support from The National Center for Atmospheric Research which is sponsored by the National Science Foundation. Funding for this Discovery mission is provided by NASA's Science Mission Directorate.

REFERENCES

Agol, E., Steffen, J., Sari, R., & Clarkson, W. 2005, MNRAS, 359, 567
Argabright, V. S., et al. 2008, Proc. SPIE, 7010, 70102
Batalha, N. M., et al. 2010a, ApJ, 713, 109
Batalha, N. M., et al. 2010b, ApJ, 713, 103
Borucki, W. J., et al. 2009, Science, 325, 709
Borucki, W. J., et al. 2010a, ApJ, 713, 126
Borucki, W. J., et al. 2010b, ApJ, submitted (arXiv:1006.2779)
Bruntt, H., et al. 2010, A&A, 519, 51
Bryson, S., et al. 2010, ApJ, 713, 97
Caldwell, D. A., et al. 2010, Proc. SPIE, 7731, 773117
Charbonneau, D., et al. 2009, Nature, 462, 891
Christensen-Dalsgaard, J. 2004, Solar Phys., 220, 137
Christensen-Dalsgaard, J. 2008a, Ap&SS, 316, 13
Christensen-Dalsgaard, J. 2008b, Ap&SS, 316, 113
Christensen-Dalsgaard, J., Arentoft, T., Brown, T. M., Gilliland, R. L., Kjeldsen, H., Borucki, W. J., & Koch, D. 2008, J. Phys.: Conf. Ser., 118, 012039
Christensen-Dalsgaard, J., et al. 2010, ApJ, 713, L164
Dunham, E. W., et al. 2010, ApJ, 713, 136
Ferraz-Mello, S., Tadeu dos Santos, M., Beauge, C., Michtchenko, T. A., & Rodriguez, A. 2010, arXiv:1011.2144
Ford, E. B. 2005, AJ, 129, 1706
Ford, E. B. 2006, ApJ, 642, 505
Fortney, J., Marley, M., & Barnes, J. 2007, ApJ, 659, 1661
French, M., et al. 2009, Phys. Rev. B, 79, 054107
Gilliland, R. L., et al. 2010, ApJ, 713, L160
Girardi, L., et al. 2008, PASP, 120, 583
Grasset, O., Schneider, J., & Sotin, C. 2009, ApJ, 693, 722
Grec, G., Fossat, E., & Pomerantz, M. 1983, Solar Phys., 82, 55
Grevesse, N., & Noels, A. 1993, in Origin and Evolution of the Elements, ed. N. Prantzos, E. Vangioni-Flam, & M. Cassé (Cambridge: Cambridge Univ. Press), 15

Hatzes, A. P., et al. 2010, A&A, 520, 93
Hayward, T. L., Brandl, B., Pirger, B., Blacken, C., Gull, G. E., Schoenwald, J., & Houck, J. R. 2001, PASP, 113, 105
Holman, M. J., et al. 2010, Science, 330, 51
Huber, D., Stello, D., Bedding, T. R., Chaplin, W. J., Arentoft, T., Quirion, P.-O., & Kjeldsen, H. 2009, Commun. Asteroseismol., 160, 74
Isaacson, H., & Fischer, D. A. 2010, ApJ, 725, 875
Jenkins, J. M., et al. 2010a, ApJ, 713, L87
Jenkins, J. M., et al. 2010b, ApJ, 713, L120
Jenkins, J. M., et al. 2010c, ApJ, 724, 1108
Jenkins, J. M., et al. 2010d, Proc. SPIE, 7740, 77400D
Johnson, J. A., Winn, J. N., Albrecht, S., Howard, A. W., Marcy, G. W., & Gazak, J. Z. 2009, PASP, 121, 1104
Koch, D. G., et al. 2010a, ApJ, 713, 79
Koch, D. G., et al. 2010b, ApJ, 713, 131
Latham, D. W., Brown, T. M., Monet, D. G., Everett, M., Esquerdo, G. A., & Hergenrother, C. W. 2005, BAAS, 37, 1340
Latham, D. W., et al. 2010, ApJ, 713, 140
Leger, A., et al. 2009, A&A, 506, 287
Mandel, K., & Agol, E. 2002, ApJ, 580, 171
Mandushev, G., et al. 2005, ApJ, 621, 1061
Marcus, R., Sasselov, D., Hernquist, L., & Stewart, S. 2010, ApJ, 712, 73
Marcy, G. W., et al. 2008, Phys. Scr..T, 130, 014001
Marigo, P., Girardi, L., Bressan, A., Groenewegen, M. A. T., Silva, L., & Granato, G. L. 2008, A&A, 482, 883
Mazeh, T. 2008, in EAS Publ. Ser. 29, Tidal Effects in Stars, Planets and Disks, ed. M.-J. Goupil & J.-P. Zahn (Paris: EDP Sciences), 1
Nettelmann, N., Fortney, J. J., Kramm, U., & Redmer, R. 2010, arXiv:1010.0277
Pfahl, E., Arras, P., & Paxton, B. 2008, ApJ, 679, 783
Pont, F., Aigrain, S., & Zucker, S. 2010, arXiv:1008.3859
Prsa, A. 2010, MNRAS, doi: 10.1111/j.1365-2966.2010.17823.x
Queloz, D., et al. 2001, A&A, 379, 279
Queloz, D., et al. 2009, A&A, 506, 303
Ragozzine, D., & Holman, M. J. 2010, arXiv:1006.3727
Robin, A. C., Reylé, C., Derriére, S., & Picaud, S. 2003, A&A, 409, 523
Rogers, L. A., & Seager, S. 2010, ApJ, 712, 974
Seager, S., & Deming, D. 2009, ApJ, 703, 1884
Seager, S., & Mallén-Ornelas, G. 2003, ApJ, 585, 1038
Seager, S., Whitney, B., & Sasselov, D. 2000, ApJ, 540, 504
Seager, S., et al. 2007, ApJ, 669, 1279
Steffen, J. H., & Agol, E. 2005, MNRAS, 364, L96
Steffen, J. H., et al. 2010, ApJ, 725, 1226
Tassoul, M. 1980, ApJS, 43, 469
Torres, G., Konacki, M., Sasselov, D. D., & Jha, S. 2004, ApJ, 614, 979
Torres, G., Konacki, M., Sasselov, D. D., & Jha, S. 2005, ApJ, 619, 558
Torres, G., et al. 2010, ApJ, 727, 24
Troy, M., et al. 2000, Proc. SPIE, 4007, 31
Twicken, J. D., Clarke, B. D., Bryson, S. T., Tenenbaum, P., Wu, H., Jenkins, J. M., Girouard, F., & Klaus, T. C. 2010, Proc. SPIE, 7740, 774023
Twicken, J. D., Chandrasekaran, H., Jenkins, J. M., Gunter, J. P., Girouard, F., & Klaus, T. C. 2010, Proc. SPIE, 7740, 77401U
Valencia, D., Ikoma, M., Guillot, T., & Nettelmann, N. 2009, A&A, 516, A20
Valencia, D., O'Connell, R., & Sasselov, D. 2006, Icarus, 181, 545
Valencia, D., Sasselov, D., & O'Connell, R. 2007, ApJ, 665, 1413
Valenti, J. A., & Fischer, D. A. 2005, ApJS, 159, 141
Valenti, J. A., & Piskunov, N. 1996, A&AS, 118, 595
Van Cleve, J., & Caldwell, D. A. 2009, Kepler Instrument Handbook, KSCI 19033-001 (Moffett Field, CA: NASA Ames Research Center)
Vandakurov, Yu. V. 1967, Astron. Zh., 44, 786 (Engl. Transl. AJ, 11, 630)
van Kerkwijk, M. H., Rappaport, S. A., Breton, R. P., Justham, S., Podsiadlowski, P., & Han, Z. 2010, ApJ, 715, 51
Vogt, S. S., et al. 1994, Proc. SPIE, 2198, 362
Welsh, W. F., Orosz, J. A., Seager, S., Fortney, J., Jenkins, J., Rowe, J. F., Koch, D., & Borucki, W. J. 2010, ApJ, 713, 145
Wu, H., et al. 2010, SPIE, 7740, 42
Zeng, L., & Sasselov, D. 2011, ApJ, submitted